Politecnico di Torino

Politecnico di Torino

Physics of Complex Systems
A.a. 2022/2023
Sessione di Laurea di Dicembre 2023

Interplay between local and global critical states in the brain

Relatori:
Carla Bosia
Giovanni Rabuffo

Candidato:
Pietro Bozzo

Contents

Abstract

The brain is a complex system organized across multiple spatial and temporal scales. Emergent cortical oscillations and slowly evolving large-scale functional states coordinate the fast neuronal spiking activity. Concurrently, the firing of a few neurons has the potential to reshape the organization of billions of others. In between these macro- and microscopic levels of observation, recurrent motifs are observed at several mesoscopic scales. Recently, it has been conjectured that the brain might operate at the edge of a phase transition, due to mounting evidence of scale-free behavior in neuronal activity. Here, we will explore the interaction between critical states at different scales of a modeled neuronal network, to set the base to understand how, were the criticality hypothesis be proven correct, the brain may extract functional advantages such as efficiency in information elaboration and transmission.

1 Introduction

The brain is one of the most striking examples of a complex system found in nature. Its activity is the product of microscopic interactions of simpler units, giving rise to coordinated behavior which displays emergent properties, ranging from motor behavior to consciousness. Neurons are generally regarded as the basic brain unit, exchanging information across a nested network in the form of electric and chemical signals. Neuronal traffic occurs within a complex biophysical environment, wherein brain tissues, chemical neuromodulators, and non-neuronal cells, including glial cells, collectively contribute structural support to the optimal functioning of neurons.

Neurons exhibit complex collective activity, organized across multiple spatial and temporal scales. Observing the brain at a larger and coarser scale reveals the presence of emergent cortical oscillations and slowly evolving large-scale functional states, which coordinate the fast neuronal spiking activity. Indeed, cortical neurons tend to display synchronized activities, giving rise to coherent brain waves that offer a basic mechanism of communication across distant neuronal populations [1–4].

Even at rest, whole-brain activity has been shown to evolve according to non-trivial dynamics, displaying recurrent network motifs corresponding to the cofluctuation of neuronal signals occurring almost simultaneously in brain regions that can be also very distant from each other [5]. These large-scale brain states are generally identified using functional connectivity (FC) measures [6]. For example, FC can be extracted by evaluating the instantaneous correlation between brain regions from functional Magnetic Resonance Imaging (fMRI) experiments measuring the slow fluctuations of oxygenated blood flow (having period of some seconds), a proxy of neuronal activity. Such groups of strongly correlated brain regions, also known as resting state networks (RSNs), have been consistently observed across several mammalian species [7–9], and their characteristic dynamics has been related to cascades of activity at the neuron population level [10].

In general, the observation of neuronal synchrony suggests that brain computations can occur at the coarse scale of mesoscopic neuronal populations [11]. However, the neuron is a complex unit, capable of performing non-linear operations, which can

have far-reaching impacts on a distributed and sometimes very large subpopulation of neurons. In fact, the firing of a few neurons has the potential to reshape the organization of billions of others, as is the case when our eyes pick up an image in a glimpse and the detection of a few photons can drastically change our entire behavior. How single neurons manage to stand out in such an intricate noisy environment, and how whole-brain phase space can reduce its dimensionality in order to produce energetically efficient outputs remain open questions.

One of the forward steps in the understanding of this multi-scale activity was envisioned when Beggs and Plenz [12] described a new operating mode observed in neuronal recordings, which they named *neuronal avalanches*. These consist of aperiodic bursts of activity spreading across the population in coordinated events characterized by scale-invariant size and duration, a property which hints at the possibility that the brain self-organizes around a critical point. In fact, a similar phenomenology of cascading avalanches was already observed in sandpile models [13], earthquakes [14], and forest fires [15], and it generally arises in systems of interconnected, nonlinear elements evolving over time around a critical state where event sizes are scale-free and thus characterized by power law distributions. These systems are often described as networks of simple units with an activation threshold, integrating inputs and then redistributing energy back into the system. Indeed, neurons operate in a similar way, i.e., integrating inputs from thousands of other neurons and, after reaching a threshold, distributing their activity back to the network in the form of electrical impulses or *spikes*. Also, it is worth noting that many of the aforementioned systems can be modeled as branching processes that organize close to a critical point [16].

In light of these observations, the *brain criticality hypothesis* has garnered significant attention in the field of neuroscience, emerging as a promising unifying physics framework for characterizing brain dynamics. Indeed, the concept of the brain operating at the edge of a phase transition holds the potential to elucidate various neurobiological phenomena, offering functional advantages, such as efficiency in information elaboration, maximal sensitivity to inputs, or large dynamical repertoires [17–21]. For example, it is well known in statistical mechanics that correlation length

exhibits a diverging behavior close to phase transitions, which may have a role in maximizing information transfer across the network.

Following these initial conjectures, scale-free avalanches have been sought and identified investigating brain activity across imaging modalities with different spatial and temporal resolutions: using local field potential (LFP), electrocorticography (ECoG), magneto- and electroencephalography (M/EEG), fMRI, and calcium imaging (Ca^{2+}) [22–33]. Therefore, it is clear that such critical dynamics intervene at various levels of brain organization. In this work, we aim to study the relation between the "local" critical state of a population of interconnected neuronal units—which can be recorded by placing a multielectrode array (MEA) of microscopic electrodes distributed on a small surface of a few mm^2—and the "global" critical activity measured via whole-brain imaging modalities (e.g., fMRI, M/EEG). Understanding the interplay between these two levels of description may shed light on the multiscale mechanisms governing brain functioning and explain how the brain efficiently communicates across micro- and macroscale.

To do so, we adopted computational-modeling techniques allowing the simulation of brain activity at both levels: local populations and whole-brain network. In general, brain simulations can be performed in bottom-up and top-down fashions. In the former, modeling starts from the microscopic scale and provides detailed biophysical descriptions of single neuronal cells, e.g., the celebrated Hodgkin-Huxley neuron model. While offering precious insights into microscopic dynamics, the resolution of such models comes at the expense of scalability: on the one hand, including all biophysical details in large networks carries an enormous computational cost; on the other hand, increasing the complexity of simulations hinders interpretability of results. Indeed, one of the great challenges of neuroscience is to develop the means to interpret and understand the huge amount of activity and signals taking place in the brain, should they ever be recorded in full detail. It should be noted that, as of today, empirical recordings of brain activity are only possible at very limited spatial or temporal resolutions. For example, electrophysiological recordings with whole-brain coverage (e.g., M/EEG) have a very good temporal resolution, $\sim$1000 Hz, but a very poor spatial resolution, $\sim$3 cm^3, whereas techniques such as fMRI

are capable of reaching $\sim$1 mm^3 resolution, at the expense of temporal resolution, which is quite poor at $\sim$0.5 Hz. Even in this best-case scenario, it is estimated that a single fMRI voxel contains around 500 thousand interconnected neurons, which form complex interactions of their own, making extremely hard the inference of the causal links between the neuronal organization and whole-brain activity.

Based on these considerations, a top-down approach to modeling offers a viable alternative for whole-brain simulations: this consists of a coarse-grained description where most microscopic details are abandoned in favor of a greater scale depiction, aimed at capturing essential features of the system. This allows us to perform whole-brain simulations, describing regions with simplified mathematical mean-field models—also referred to as neural mass models (NMMs) [34, 35]—and studying their interactions. In such models, each region is described by a set of a few differential equations governing the local dynamics of a neuronal population (e.g., the mean membrane potential). Such populations are then coupled through neuroanatomical links, whose weights can be empirically measured, effectively yielding a set of coupled differential equations. The numerical resolution of this system allows the simulation of whole-brain activity in terms of region-level signals that can eventually be compared to empirical recordings. In this work, we adopt a top-down mean-field approach, connecting together neural populations individually tuned around a critical point to represent *local criticality*, coupling them via empirical structural connectivity links extracted from mice experiments, and simulating critical-like whole-brain activity, *global criticality*. Using this setup we explore how the global critical dynamics unfolding over a realistic connectome impact the local critical dynamics of neuronal populations within a brain region.

2 The criticality hypothesis

The hypothesis that the brain operates at the edge of a phase transition originated from the observation of neuronal avalanches, i.e., short-lived aperiodic bursts of neuronal activity involving distributed networks, whose size and duration follow a scale-free distribution [12]. In this section, we provide an overview of the substantiating evidence for the brain criticality hypothesis, followed by an examination of its theoretical underpinnings. While the precise nature of such transition is still debated, several models have been proposed, generally positing the critical point between a highly ordered phase and a disordered one. Roughly speaking, these phases correspond to periods of high activity and quiescence. However, as discussed at the end of this chapter, a more nuanced understanding of the hypothesized phase transition may offer a more robust account of empirical evidence.

2.1 Evidence for avalanche behavior in neuronal networks

The idea that brain networks could be operating in between phases was already suggested by several modeling studies simulating criticality in neuronal networks [36–39].

Conducting MEA experiments *in vitro*, Beggs and Plenz made the remarkable discovery of synchronized bursts of neural activations cascading through the brain network in scale-free patterns, whose statistics resemble the sandpile avalanches originally studied in the context of self-organized criticality (SOC) [40]. For this reason, these salient neuronal events were termed neuronal avalanches.

In general, the algorithm to extract neuronal avalanches from brain data consists of a binarization that focuses on rare salient events. In order:

- Raw data is collected from several brain sites, e.g., in the form of electric potentials; for each source, the signal is z-scored by subtracting its mean and dividing it by its variance.

- The z-scored signals are binarized by assigning 1 to each time point where the signal surpasses a fixed threshold and 0 otherwise. Such threshold is generally

considered around 3 standard deviations, resulting in a sparsification of the data with only a minority of "active" above-threshold data points.

- A temporal coarse-graining is applied by dividing each binarized signal into time bins of equal size and assigning 1 to time bins containing at least one activation, 0 otherwise. A standard choice for the bin size corresponds to the average inter-event interval, i.e., the average time between two consecutive activity events. However, different choices can be applied depending on the imaging modality [41].

- Avalanches are defined as sets of contiguous time bins where at least one of the recorded units is active; their size corresponds to the number of such active units, whereas their duration is identified as the number of active bins.

Using this definition, Beggs and Plenz [12] showed that the avalanche size distribution, $P(S)$, obeys a power law of the form $P(S) = S^{-\tau}$, with τ measured to be 3/2. This result was robustly observed, independently of the size of the electrode array used for measurements. Also, as expected, the distribution featured a cutoff for values of the size S approaching the instrument size, again consistently with different sizes of the measurement arrays, suggesting that the law would be range-free for an infinite array. Moreover, as theory predicted [16], avalanche duration distribution, $P(T)$, followed a power law with an exponential cutoff, with an initial slope given by $P(T) = T^{-\alpha}$, $\alpha = 2$.

This discovery set in motion the look for more evidence of such behavior across other imaging modalities, which was expected across a wide range of spatial and temporal scales, in virtue of the scale-free nature of critical phenomena. In fact, evidence of critical avalanches was found in LFP recordings [22–25] (which have a spatial resolution in the range of some millimeters and recording frequency of around 300 Hz), as well as in modalities capable of covering the entire brain, including eletrocorticography [26], ($\sim$1 cm^3 spatial resolution, 200 Hz sampling frequency), M/EEG [27–29] ($\sim$3 cm^3, 1000 Hz), fMRI [30–32] ($\sim$1 mm^3, 0.5 Hz), and calcium imaging [33] ($\sim$1 μm, 1000 Hz).

2.2 Self-organized criticality

Self-organized criticality (SOC) is a phenomenon observed and named by Bak et al. [40] to describe those systems that spontaneously organize into a critical state, in contrast to typical second-order phase transitions, where scaling behavior occurs only when a parameter is fine-tuned close to a critical value. Bak and colleagues introduced this concept when studying a cellular automaton model, known today as the sandpile model. It features a two-dimensional lattice hosting cells that can hold up to three grains of sand before toppling. When a fourth grain is added, a site is driven over the threshold and topples, distributing one grain to each of its neighboring cells, which will cause any of them to topple if it has reached the threshold. Bringing the system out of equilibrium by slowly adding grains of sand, the sandpile approaches a critical slope, where a single grain of sand can trigger sand cascades of variable sizes. At this critical point, the distribution of cascade sizes approaches a power law. In other words, no predominant temporal or spatial scale can be identified for these events, whereby in this regime cascades of different sizes and durations spontaneously occur, triggered by microscopic fluctuations. It has been argued that sandpile models share a number of features with systems having many absorbing states [42], and certain self-organized forest-fire models are related to dynamical percolation [43]. Morevore, the essential ingredients to obtain this behavior should be many nonlinear threshold units connected to each other and a separation of driving and relaxation time scales, such that the addition of sand (the driver) occurs very slowly relative to the duration of avalanches (relaxation) [44].

In fact, neurons within a network can be thought of as coupled, nonlinear threshold units: a neuron fires after receiving above-threshold inputs, then an action potential is generated and propagates through its axon, at the end of which synapses connect it with the target neurons, to which the signal is transmitted. Such connections can be excitatory or inhibitory (i.e., they can increase or decrease the excitation state of the target) but in both cases target neurons integrate the receive signals and fire once a threshold is reached. Upon firing, they redistribute activity to the network and enter a refractory period.

Beggs and Plenz proposed a branching process close to its critical point as a model to describe the spreading of avalanches in a neuronal network. A branching process is a stochastic process in which every active unit has, on average, probability σ, the branching parameter, to spread its active state to its neighbors. Therefore, σ can also be interpreted as the average fraction between active units at a time step and at the previous one. For values of σ lower than 1, the activity evoked by a random supra-threshold activation will die out quickly, whereas for values greater than 1 it will explode and reach the size of the whole network. It is for values close to 1 that a critical evolution of the process is observed, as activity will proceed somehow constantly, until stochastic fluctuations will cause instantaneous σ to momentarily be close to zero, interrupting it. Every time this happens, an avalanche is ended, and, owing to stochastic fluctuations, avalanche events can start spontaneously, propagate through the network, and die out after a variable lifetime with no characteristic scale. Therefore, the network is thought to operate in the transition between an absorbing state, where all units are inactive, and a non-zero activity phase.

2.3 Mean-field directed percolation

Branching processes belong to the directed percolation (DP) universality class, as stochastic transmission models having a unique absorbing state and no further symmetries usually do [45–47]. Furthermore, if the network has a topological dimension above 4, such as random or complete graphs, the model usually belongs to the mean-field directed percolation (MF-DP) universality class, a special case of DP for which critical exponents values can be analytically determined owing to its mean-field nature.

The values of the exponents of the power laws registered by Beggs and Plenz in 2003 matched very closely those predicted by statistical mechanics theories for a DP process. Correspondence in numerical values is a very significant discovery, as renormalization group theory states that values of the critical exponents—i.e., exponents describing the behavior of physical quantities near continuous phase transitions—are determined by the general properties of the system under study. In particular,

different systems can exhibit the same behavior close to a critical point, i.e., close to specific values of macroscopic parameters that govern the transition between different states of the system. This is because, as a result of the interaction between countless simple units, emergent behavior does not strictly depend on microscopic details of the system, but is rather characterized by general aspects of the ensemble phenomenon. Therefore, it is said that systems displaying the same critical behavior, in spite of different microscopic organizations, belong to the same universality class, which is characterized by its critical exponents values, among other properties.

An experimentally verified branching parameter close to 1 strengthened Beggs and Plenz's claim. To evaluate it, they defined d as the ratio between active units in a time bin of an avalanche and its predecessor. it was computed for every pair of consecutive bins, to then compute its expected value:

$$\sigma = \sum_{d} d\ p(d) \tag{1}$$

Note that, in their work, $p(d)$ differed from the simple empirical frequency of d for a factor introduced to correct for the refractory period of recording electrodes; this will not be reported here for the sake of simplicity.

Nonetheless, to resize the plausibility of such a claim, Touboul and Destexhe [48] argued that power-law distributions alone are insufficient hallmarks of a critical phase transition, as they are observable in non-critical systems as well. They suggested a fundamental scaling relation was to be tested, the so-called crackling noise relation. Crackling is a phenomenon in which systems react with discrete events of a variety of sizes to slow changes in external inputs [49]. For instance, violent and intermittent earthquakes are generated as two tectonic plates slowly contact one another, a magnetic material in a changing external field magnetizes in a series of jumps, or a piece of paper emits intermittent, sharp noises ("crackling noise") as it is slowly crumpled. These individual events span many orders of magnitude in size, showing no characteristic size scale. Considering all avalanches of a certain duration T in an experiment, they will have a distribution of sizes S, $P_T(S)$, centered around an average $\langle S \rangle(T) = \int S\ P_T(S)\ \mathrm{d}S$. Assuming that the system fulfills scale invariance,

such average values at different spatial and temporal scales should be the same. This can be expressed as:

$$\langle S\rangle(T) = A\,\langle S\rangle(T/B) \tag{2}$$

where A and B are scaling factors for space and time, respectively. Considering the timescale to be expanded by a small factor $B = 1/(1-\delta)$, it is safe to assume that the rescaling of the size will also be small, as $A = 1 + a\delta$. Hence:

$$\begin{aligned}
\langle S\rangle(T) &= (1+a\delta)\langle S\rangle((1-\delta)T) \qquad (3)\\
\langle S\rangle(T) &= \langle S\rangle((1-\delta)T) + a\delta\langle S\rangle((1-\delta)T)\\
a\delta\langle S\rangle((1-\delta)T) &= \langle S\rangle(T) - \langle S\rangle(T-\delta T)\\
a\langle S\rangle((1-\delta)T) &= T\frac{\langle S\rangle(T) - \langle S\rangle(T-\delta T)}{\delta T}\\
a\langle S\rangle(T) &= T\frac{\mathrm{d}\langle S\rangle}{\mathrm{d}T}, \qquad (4)
\end{aligned}$$

assuming δ to be small. Such expression admits the solution:

$$\langle S\rangle(T) = S_0 T^a, \tag{5}$$

where the critical exponent a is a universal prediction of a given theory. Considering the DP universality class, scaling theory shows that $a = 1/\sigma\nu z$, i.e., a combination of other critical exponents, and provides the scaling relation mentioned above as the crackling-noise relation (see [49]):

$$\frac{\alpha - 1}{\tau - 1} = \frac{1}{\sigma\nu z}. \tag{6}$$

This relation is crucial as its validity is necessary to propose that an observed neuronal activity pattern is indeed a hallmark of a phase transition.

Afterward, there have been studies producing similar findings in voltage imaging recordings of the mouse cortex [50] and in two-photon imaging of the rat cortex [51], in which MF-DP critical exponents were accurately retrieved. However, other experimental results disagreed on the exponents values, such as *ex-vivo* recordings

of the turtle visual cortex [52], spike avalanches of rats under ketamine-xylazine anesthesia [53] or M/EEG recorded avalanches in humans [28, 54], among others. Nonetheless, Carvalho et al. [55] showed that exponents possibly differ from those predicted by the MF-DP universality class due to subsampling effects.

As a final remark, it is worth noting that since many kinds of systems can belong to the same universality class, thus producing the same critical exponents and scaling relations, branching processes are not the only candidate models to describe avalanche spreading in neuronal networks. As a matter of fact, the quiescent-to-active transition interpretation these models imply has been challenged because too simplistic to explain the complex repertoire of dynamics observed in neural recordings. Moreover, SOC models rely on the hypothesis of an extremely large separation of dynamical timescales, as mentioned above, which might not be a realistic assumption for neuronal networks [56, 57].

2.4 Advantages of critical behavior

What advantages could an avalanche operating mode bring to a neuronal network? From an analytical perspective, an important consequence of power law distributions is that they are heavy-tailed, meaning that realizations drawn from these distributions are not concentrated around their mean. This appears evident from an explicit calculation of the expected value, which is diverging for values of the exponent lower than 2, as shown by:

$$\langle S \rangle = \int S\ P(S)\ \mathrm{d}S = \int_{S=S_0}^{S=\infty} S\ S^{-\alpha}\ \mathrm{d}S = \int_{S=S_0}^{S=\infty} S^{1-\alpha}\ \mathrm{d}S. \tag{7}$$

This implies that avalanches of every length are expected, even though shorter ones will be more likely, and this has consequences on maximizing information transmission, as shown in [12, 19, 58].

Moreover, in their first paper covering the topic [12], Beggs and Plenz simulated a feed-forward neural network architecture embedded in a random graph, where each edge has probability p_i to transmit activity to its target node, and found that

configurations that reproduced values of σ close to 1 maximized information transmission. It is worth noting that the choice of a feed-forward network was supported in their case by the nature of the tissue they were studying. Also, when a recurrent branching network is tuned to the critical point, the number of significantly repeating avalanche patterns is maximized [59], which may contribute to optimal information storage. This idea can be intuitively understood by considering that scale-invariance involves complex patterns, akin to those seen in fractal shapes. Maximum storage capacity may be found within these intricate patterns.

Similarly, through the variation of synaptic weights variance in a spiking network model, Bertschinger and colleagues [58, 60] generated networks with damped, sustained, and expanding activity. When the variance of synaptic strengths is low, the activity originating from a specific neuron results in downstream effects that are relatively consistent, leading to stable activity patterns. Conversely, when such variance is high, the activation of downstream targets by a single neuron varies with each occurrence, giving rise to highly unpredictable activity patterns. This study revealed that computational processes rely on a delicate balance between order and variability. In instances where a network exhibits excessive order, it is constrained in its ability to perform diverse mappings between inputs and outputs, thereby limiting its computational capacity. On the other hand, if randomness in a network is exaggerated, this may have a broader range of mappings, but their reliability is compromised, ultimately hindering effective computation.

Finally, Shew et al. [61] performed *in-vivo* experiments as well as computational simulations to measure the relation that occurs in a neuronal network between information transmission and a statistical index, κ, which they used to measure the distance of the observed distribution of events from avalanche behavior. Their results showed that entropy and information transmission are maximized for $\kappa \approx 1$, a condition under which neuronal avalanches emerge. For a more detailed review of how avalanche behavior can be shown to maximize dynamic range, information transmission, and information capacity, readers can refer to [18].

3 Modeling a critical brain

Modeling the scale-invariant behavior observed in neural tissues through neuronal network simulations opens up the possibility of reproducing the phenomenology of critical avalanches, studying the system's features as functions of the model parameters, and addressing theoretical questions about the brain's organizational principles. In this chapter, we will introduce brain models aimed at addressing a specific open question: how does the "global" criticality measured at the whole-brain level (e.g., via M/EEG) relate to the "local" criticality measured at the level of small cortical patches (e.g., via MEA)?

As mentioned before, experimental measures of global and local criticality rely on technologies capable of different spatial and temporal resolutions. In most cases, the local scale includes fine-grained details about neuronal activity, whereas the global scale is studied at a coarser spatiotemporal resolution of mesoscopic populations. Similarly, in theoretical models, the local scale is generally described as a densely connected neuronal network, whereas the global scale can be modeled as mesoscopic neural masses connected via structural connections. In either case, the choice of which details are to be included in the model impacts its predictive power, computational feasibility, and interpretability of results.

In the following sections, we will describe brain models reproducing critical-like behavior across these different scales. Finally, we will link the two scales, thereby addressing the multiscale mechanisms of criticality in the brain.

3.1 The microscale: neuronal network models

A local neuronal population can be modeled at the microscopic level as a neuronal network of densely connected neurons. Since synchrony is a recurrent feature of neural recordings, a standard modeling choice is the phenomenological phase synchronization model: the Kuramoto model. It consists of a population of N coupled

phase oscillators described by $\varphi_i(t)$ whose dynamics are governed by

$$\dot{\varphi}_i(t) = \omega_i + \sum_{j=1}^{N} K_{ij} \sin\left[\varphi_i(t) - \varphi_j(t)\right], \quad i = 1, \ldots, N, \tag{8}$$

where ω_i is the natural frequency of the i-th oscillator, drawn from a distribution $p(\omega)$, and K_{ij} is the coupling strength between units i and j. Here, each neuron is modeled as a phase oscillator, i.e., a point confined on the unit circle, spontaneously rotating at a specific natural frequency, while the coupling tends to synchronize it with all the others. When the coupling is sufficiently weak, the oscillators run incoherently, whereas beyond a certain coupling threshold collective synchronization emerges. A particularly simple case, amenable to in-depth analytical analysis, is that of the mean-field coupling between oscillators, i.e., $K_{ij} = J/N > 0,\ \forall\ i, j$. In this case, it is convenient to define the Kuramoto order parameter:

$$Z(t) = \langle e^{i\varphi_j(t)} \rangle_j = \frac{1}{N} \sum_{j=1}^{N} e^{i\varphi_j(t)} = R(t) e^{i\psi(t)}, \tag{9}$$

where $R(t) \in [0, 1]$ measures the coherence of the oscillator population and $\psi(t)$ the average phase. Under this definition, Eq. 8 can be written as:

$$\dot{\varphi}_i(t) = \omega_i + JR(t) \sin\left[\psi(t) - \varphi_i(t)\right], \tag{10}$$

which reveals that oscillators are coupled to the common average phase $\psi(t)$ through a coupling coefficient given by $JR(t)$.

In the thermodynamic limit, $N \to \infty$, units may be expected to be distributed according to a probability density $\rho(\varphi, \omega, t)$, leading to the following definition of the order parameter:

$$Z(t) = \int_{-\pi}^{\pi} e^{i\varphi} \left(\frac{1}{N} \sum_{j=1}^{N} \delta(\varphi - \varphi_j) \right) \mathrm{d}\varphi = \int_{-\pi}^{\pi} \int_{-\infty}^{+\infty} e^{i\varphi} \rho(\varphi, \omega, t) p(\omega) \mathrm{d}\varphi \mathrm{d}\omega, \tag{11}$$

where the first identity is a convenient rewriting of the definition of Z and the second

one stems from writing the sum as an integral in the continuous limit. This equation illustrates how Z provides information on the oscillators' synchronization. Indeed, two significant limits can be identified:

$$J \to 0 : \quad \varphi_i(t) = \omega_i t + \varphi_i(0), \tag{12}$$

the uncoupled limit, in which the integration of Eq. 10 easily provides the evolution of $\varphi_i(t)$ and, thus, letting $\varphi \approx \omega t$ in Eq. 11 yields $R(t) \to 0$ as $t \to \infty$, implying that oscillators are not synchronized. In the opposite case,

$$J \to \infty : \quad \varphi_i(t) \approx \psi(t) \; \forall \; i, \tag{13}$$

the strong coupling limit, oscillators become synchronized to the average phase $\psi(t)$ and thus Eq. 11 gives $R(t) \to 1$ for $t \to \infty$ [62].

Disregarding node heterogeneity and adding a noise term, which is a customary ingredient in modeling neural dynamics, a simpler yet meaningful model is obtained, named the annealed Kuramoto model, which reads:

$$\dot{\varphi}_i(t) = \omega + \frac{J}{N} \sum_{j=0}^{N} \sin[\varphi_j(t) - \varphi_i(t)] + \sigma n_i(t), \quad i = 1, \ldots, N. \tag{14}$$

In it, ω is a common intrinsic frequency, $n_i(t)$ is a zero-mean unit-variance Gaussian white noise multiplied by the noise amplitude σ, and J is the constant coupling strength among all neighbors on a fully connected network. Eq. 14 exhibits a synchronization phase transition where the synchronization (Kuramoto) order parameter $Z(t) = \langle e^{i\varphi_j} \rangle_j$ experiences a supercritical Hopf bifurcation from a fixed point to a limit cycle, revealing the emergence of collective oscillations [62, 63]. However, computational analyses revealed that neither at the critical point of Eq. 14 nor around it scale-free avalanches can be found, even though, as expected for phase transitions, other standard quantities are known to exhibit scale-invariant behavior [64].

Buendía et al. [64] proposed a variant of the annealed Kuramoto model, Eq. 14, capable of displaying scale-free avalanches in concomitance with incipient os-

cillations. In it, every node is modeled by Eq. 15, as its dynamical evolution is an oscillation with a phase-dependent angular velocity, a characteristic feature of *spike-like* behavior.

$$\dot{\varphi} = \omega + a \sin \varphi \tag{15}$$

As a remark, a system is described as *excitable* when it presents a single, stable equilibrium, but a sufficiently strong input can drive the system in a large excursion in phase space before returning to the stable fixed point [65–67]. In describing neuronal models, different *excitability classes* have been named, among which type-I excitability is characterized by the continuous growth of the spiking rate when the input current is continuously increased, while type-II excitability involves a sudden jump in the spiking rate under the same circumstances. In bifurcation theory, type-I excitability arises when the corresponding limit cycle appears with a vanishing frequency, i.e., infinite-period bifurcations, whereas in type-II excitability limit cycles emerge with a finite, nonvanishing frequency [65].

In Eq. 15, which is the canonical form of type-I excitable units, the parameter a is named excitability. For $a > \omega$ the deterministic dynamics of each isolated unit exhibits a stable fixed point at $\varphi^* = -\arcsin(\omega/a)$, as well as a saddle point at $-\varphi^*$. The addition of a stochastic term $\sigma n(t)$ can induce fluctuations beyond the saddle, thus generating large excursions of the phase before relaxing back to its equilibrium. Conversely, for $a < \omega$, the system oscillates with phase-dependent angular velocity and, as the saddle-node into invariant circle (SNIC) bifurcation point $a_c = \omega$ is approached, the frequency of the oscillations vanishes, implying that the period becomes infinite, while the amplitude remains constant.

Thus, introducing noise and standard Kuramoto coupling, the whole model on a fully connected network reads:

$$\dot{\varphi}_i(t) = \omega + a \sin \varphi_i(t) + \frac{J}{N} \sum_{j=0}^{N} \sin[\varphi_j(t) - \varphi_i(t)] + \sigma n_i(t). \tag{16}$$

Computational simulations of a fully connected network of $N = 5000$ neurons produce the phase diagram in Fig. 1. It reveals that there are two main types of

collective dynamical regimes: oscillations, i.e., synchronous states, in the lower-left region, and stable fixed points, corresponding to either high-activity asynchronous states in the upper part of the diagram or low-activity states in the lower-right part. These low-activity states are characterized by susceptibility to collective reaction to external inputs and constitute the so-called collective-excitability phase. Furthermore, where the three phases meet, a fourth, triangular region displaying bistability is found and, at the crossing between that and the synchronous region, scale-invariant avalanches can be identified.

3.2 The mesoscale: mean-field models

The complex patterns observed in large-scale experimental recordings include collective oscillations emerging out of neural synchronization, as well as highly heterogeneous (avalanche-like) outbursts of activity interspersed by periods of quiescence. In search for a mean-field model capable of reproducing such patterns of activity, di Santo et al. employed a Landau-Ginzburg (LG) model to describe the mean-field behavior of the fundamental units capable of scale-invariant whole-brain oscillations

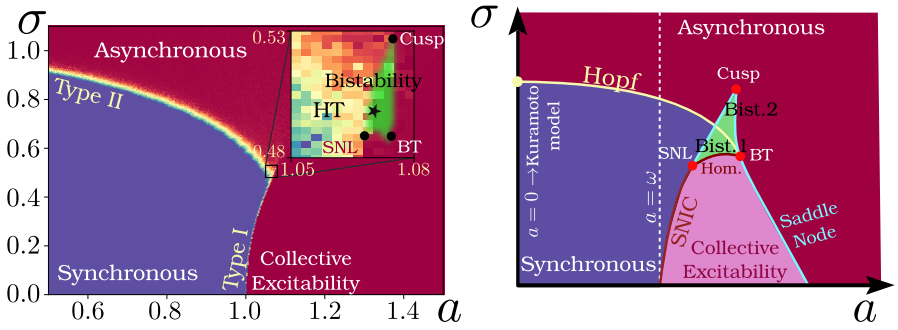

Figure 1: a) Phase diagram and bifurcation lines of the type-I excitable Kuramoto model, Eq. 16, computed via simulations on a fully connected network of $N = 5000$ units, setting $\omega = 1$, $J = 1$. The bistability region was identified by solving numerically Eq. 24, assuming $Z_{51} = 0$. In the inset, the bistability region is shown and a star marks a point where scale-free avalanches were detected. b) Sketch of the analytically derived phase diagram for the mean-field approximation of Eq. 16. The bistability region, whose size has been increased for clarity, is drawn in green, delimited by three transition lines and three vertices: the BT point, the SNL and the cusp. *FIG. 1 and 2 of* [64].

[68].

Landau and Ginzburg pioneered the study of phases of matter and their transitions with a parsimonious, coarse-grained approach, in which most microscopic details are safely neglected. The addition of space-dependent fluctuations to describe inhomogeneous systems completes the picture, creating a solid theory for phase transitions. Following a similar approach, di Santo et al. proposed a model in which two state variables describe the neural population: the excitatory activity, ρ, and the available synaptic resources, R. The dynamical evolution of the first variable follows an equation already proposed by Wilson and Cowan [69], which is a power series truncated to the third order, as prescribed by Landau's principle of parsimony:

$$\dot{\rho}(t) = [-a + R(t)]\rho(t) + b\rho^2(t) - \rho^3(t) + h, \tag{17}$$

where $a > 0$ controls the spontaneous decay of activity, balanced by new activity generated proportionally to available synaptic resources. $b > 0$ controls nonlinear integration effects, while the cubic term imposes saturation of the activity, preventing its unbounded growth, and h models an external driving field. The second variable follows a well-known equation modeling synaptic plasticity proposed by Tsodyks and Markram [70]:

$$\dot{R}(t) = \frac{1}{\tau_R}(\xi - R(t)) - \frac{1}{\tau_D}R(t)\rho(t), \tag{18}$$

where ξ is the baseline level of synaptic resources and τ_R, τ_D are the characteristic recovery and depletion times. It is worth noting that the equation for the activity ρ is the minimal form of a first-order phase transition with hysteresis or saddle-node bifurcation, upon fixing the number of synaptic resources R. It displays a quiescent or "down" state $\rho = 0$ when $R \leq a$ and an active or "up" state for $R > a$. On the other hand, the second equation accounts for the dynamics of the level of synaptic resources and includes a slow recovery term, dominating when activity is low, and a fast consumption one, which dominates the dynamics in the presence of activity $\rho \neq 0$.

Analyzing Eqs. 17 and 18 it is possible to show that the system behavior depends

on the value of the maximum allowed synaptic resources, ξ. For $\xi < a$, the only fixed point is a quiescent state of low activity. For larger values of ξ, the two nullclines intersect at an unstable fixed point, giving rise to a limit cycle, i.e., to relaxation oscillations in which both $\rho(t)$ and $R(t)$ oscillate. If ξ is large enough, an "up" state emerges: a fixed point with nonvanishing activity. At $\xi_c = a$ an infinite-period homoclinic bifurcation into a limit cycle is observed. Finally, as the control parameter ξ is further increased, one encounters another homoclinic bifurcation at which the limit cycle disappears, giving rise to an "up" fixed point. Isolated units of this LG model can produce spikes even when they are slightly below the threshold owing to the effect of noise; in other words, they behave as type-I excitable units. As a remark, we note that type-I excitability can rely either on a SNIC bifurcation, as in equation Eq. 15, or on a homoclinic bifurcation, as in this LG model. Both cases exhibit the common relevant feature of generating spike-like infinite-period oscillations at the bifurcation point [65].

Another noteworthy mean-field model can be obtained analytically from the model described in the previous section, Eq. 16, which also allows for a more in-depth understanding of its phase diagram. Furthermore, through a mean-field approach, a mesoscale description of an ensemble of spike-like oscillators can be derived, allowing the description of a neuron population in terms of a few mean-field variables.

In the following, the derivation of the mean-field model for Eq. 16 is presented. Parameters ω and J are considered to be fixed to 1; a choice which can be shown not to impact the results [64]. Owing to the presence of the term $a\sin(\varphi_i)$, which induces even uncoupled units to spend more time around some particular phase values, the simple average Z is inadequate to describe the collective state of the system and, thus, cannot allow to correctly identify synchronization. In order to circumvent this problem analytically, it is convenient to consider the hierarchy of higher-order moments of the variable $e^{i\varphi_j}$, the so-called Kuramoto-Daido parameters:

$$Z_k = \langle e^{ik\varphi_j} \rangle_j = \frac{1}{N} \sum_{j=0}^{N} e^{ik\varphi_j} = R_k e^{i\psi_k}, \quad k \in \mathbb{N}. \tag{19}$$

Using standard trigonometric relations, Eq. 16 can be rewritten as a function of $Z_1(t) = R_1(t)e^{i\psi_1(t)}$, leading to the following set of Langevin equations:

$$\dot{\varphi}_j(t) = \omega + a\sin\varphi_j(t) + JR_1(t)\sin[\psi_1(t) - \varphi_j(t)] + \sigma n(t), \tag{20}$$

in which the mean-field nature of the coupling is evident.

In order to solve these equations, the first step is to consider a large number of oscillators $N \to \infty$, so that the system can be described in the continuum limit using the probability density to find an oscillator around any given phase value φ, $P(\varphi)$. The evolution of such probability density is governed by the following Fokker-Planck equation:

$$\partial_t P(\varphi, t) = \frac{\sigma^2}{2}\partial_\varphi^2 P(\varphi, t) - J\partial_\varphi[(\omega + a\sin\varphi + \frac{Z_1 e^{-i\varphi} + \overline{Z}_1 e^{i\varphi}}{2i})P(\varphi, t)]. \tag{21}$$

Here, $R_1\sin(\psi_1 - \varphi) = (Z_1 e^{-i\varphi} + \overline{Z}_1 e^{i\varphi})/2i$ has been used. Due to its periodicity, it is convenient to expand the probability density $P(\varphi, t)$ in Fourier series:

$$P(\varphi, t) = \frac{1}{2\pi}\sum_{k=-\infty}^{+\infty} p_k(t)e^{ik\varphi}, \tag{22}$$

where $p_k = \bar{p}_{-k}$. It can be shown that the Kuramoto-Daido parameters can be mapped onto the Fourier coefficients:

$$Z_k = \int_0^{2\pi} P(\varphi, t)e^{ik\varphi}\mathrm{d}\varphi = p_{-k}. \tag{23}$$

Plugging the series expansion, Eq. 22, into the Fokker-Planck equation yields an infinite set of differential equations, one for each of the parameters Z_k. To obtain them, after performing the derivatives, all the terms must be written as $(2\pi)^{-1}\sum_k f(Z_k, Z_{k+1}, Z_{k-1}, \ldots)e^{ik\varphi}$ for some function f. Then, since the exponentials $e^{ik\varphi}$ are the Fourier-basis elements, all parameters can be identified mode by mode, leading to an equation for the evolution of each Kuramoto-Daido order pa-

rameter. The resulting set of equations,

$$\dot{Z}_k Z_k(i\omega k - \frac{k^2\sigma^2}{2}) + \frac{ak}{2}\left(Z_{k+1} - Z_{k-1}\right) + \frac{Jk}{2}\left(Z_1 Z_{k-1} - \bar{Z}_1 Z_{k+1}\right), \tag{24}$$

constitutes a complete description of the system. In order to proceed analytically, given that all equations are coupled, a closure is needed to truncate the infinite hierarchy. In the literature, different low-dimensional closures have been explored, the simplest of which is the well-known Ott-Antonsen (OA) ansatz, which amounts to expressing each moment as a power of the first:

$$Z_k(t) = \left[Z(t)\right]^k. \tag{25}$$

This scheme becomes exact in a deterministic, noise-free system. In general, using the OA ansatz and letting $Z(t) = R(t)e^{i\psi(t)}$ leads to the following mean-field equations:

$$\begin{aligned} \dot{R} &= \frac{1}{2}R\left[J\left(1-R^2\right) - \sigma^2\right] - \frac{1}{2}a\left(1-R^2\right)\cos\psi, \\ \dot{\psi} &= \omega + \frac{a\left(1+R^2\right)\sin\psi}{2R}, \end{aligned} \tag{26}$$

which describe the system at an approximation of order $O(\sigma^2)$ [71]. Remarkably, these equations match those obtained by Childs and Strogatz in the case of deterministic oscillators with heterogeneous frequencies distributed as a Lorentzian [72]. Indeed, the OA ansatz is equivalent to the assumption of a Lorentzian distribution for the angles: assuming $P(\varphi, t)$ to be a Lorentzian distribution, and following the same procedure, one recovers the OA ansatz result. Furthermore, it is worth noting that, for a fixed value of R, the equation of the collective phase ψ is the normal form of a saddle-node into an invariant circle (SNIC) bifurcation. On the other hand, the equation for $\dot{R}$ is almost the same as in the annealed Kuramoto model, with the addition of a perturbation proportional to the excitability parameter a.

Using this mean-field description, it is possible to analytically obtain a phase diagram for the type-I excitable oscillators model, reported in Fig. 1. This confirms

the presence of three phases for the system: a synchronous one, a high-activity asynchronous regime, and a collective-excitability phase, separated by different types of bifurcation lines. In particular, for low noise amplitudes σ, as the control parameter a is increased, there is a collective SNIC bifurcation from the oscillatory regime to a phase characterized by a stable fixed point with very low spiking activity, but susceptible to collectively react to external inputs: the collective-excitability phase. In analogy with the classification of excitability types, this is called type-I synchronization transition, as oscillations emerge at the transition point with zero frequency (infinite period) and finite amplitude. On the other hand, for small values of a, by increasing σ, a collective Hopf bifurcation to a high-activity asynchronous state is encountered. It is referred to as a type-II synchronization transition, since oscillations arise with a fixed nonvanishing frequency. Remarkably, due to topological reasons [65], the aforementioned type-I and type-II bifurcation lines do not intersect, meaning there is no such thing as a "tricritical" point. Instead, in the region where they come close to each other, the triangular-shaped region of bistability shown by simulations is retrieved, delimited by three bifurcation lines and three codimension-2 bifurcations. In particular, there are:

- A Bognadov-Takens (BT) point, where the Hopf-bifurcation line finishes, colliding tangentially with a line of saddle-node bifurcations,
- A saddle-node-loop (SNL) where the line of SNIC bifurcations ends, becoming a standard saddle-node line,
- A cusp, where the two saddle-node bifurcation lines collide.

As a further remark, the bistability region is divided into two halves by the Hopf-bifurcation line, so that the regime of collective excitability coexists with either oscillations below the Hopf line or the high-activity asynchronous state above it. In other words, in this region, the Hopf bifurcation occurs in one of the branches of two coexisting solutions, i.e., in concomitance with bistability. Notably, the nontrivial triangular-shaped structure described above is rather universal and emerges in other models displaying both type-I and type-II transitions, such as the broadly used

Wilson-Cowan model of excitatory-inhibitory networks [73]. Furthermore, the peculiar phenomenology of collective excitability alongside codimension-2 bifurcation points is not model-specific and has been featured in various models for neuronal activity [74].

To summarize the important implications of this model, one can state that general synchronization transitions must be analyzed considering not just the standard type-I and type-II cases, but also more complex scenarios, including the case in which the transition to synchrony occurs in concomitance with bistability, i.e., when incipient oscillations coexist with low-activity asynchronous states. Such a scenario has been named hybrid-type (HT) synchronization transition and allows for a richer phenomenology, owing to the presence of codimension-2 bifurcations and bistability. It has been hypothesized [64] that the above-described LG theory, and possibly other models [75], exhibit scale-free avalanches at the edge of synchronization precisely because some kind of bistability is present around the synchronization transition.

As a final remark, an aspect of this model that might need to be revisited is that here there are no true absorbing states, i.e., states from which the system cannot exit, neither as a consequence of the deterministic dynamics nor as the result of stochasticity. Usually, absorbing states are expected when the noise is multiplicative, as was the case for the LG model, meaning that noise amplitude is proportional to activity and thus vanishes in its absence. This requires a well-defined zero activity state, which cannot be easily implemented in Eq. 16 due to the periodicity of the phase state variable. On the other hand, it is well established that absorbing states are needed to generate branching-process exponents [76]. Thus, further work is still needed to elucidate what happens in these kinds of modeling approaches if absorbing states are included.

3.3 The macroscale: connectome-based models

Reducing the complexity of the brain is essential to achieve an effective description of large-scale neuronal networks for critical behavior. To this end, the brain can be parceled into regions of interest (ROIs), which usually correspond to anatomical

regions of the brain. This allows to represent the whole brain as an ensemble of few discrete interacting elements. Each region is treated as a point in space, described by a few state variables bound to follow dynamical equations, coupled to each other in a structural network. Equations describing the behavior of nodes can be obtained based on phenomenological considerations or through mean field approximations of microscopic single-neuron models.

The graph in which the model is embedded may be a 2D one, when anatomical considerations support it, or an empirically extracted connectome, i.e., a weighted graph in which each weight represents the connection strength between two nodes, based on experiments which measure how much couples of selected regions interact. Using this approach and calling $\boldsymbol{x}_i = (x_i, y_i, ...)$ the vector of state variables of region i, entries W_{ij} of the connectome customarily enter the coupled differential equations for state variables in the following way:

$$\dot{\boldsymbol{x}}_i(t) = \boldsymbol{f}_i(\boldsymbol{x}_i) + G \sum_{j \neq i} W_{ij}\, \boldsymbol{g}(\boldsymbol{x}_i, \boldsymbol{x}_j) \tag{27}$$

where $\boldsymbol{f}_i$ governs the uncoupled dynamical evolution of $\boldsymbol{x}_i$, G is the global coupling constant, determining the amount of the impact of the network coupling on the evolution of its units, and $\boldsymbol{g}$ is some pairwise interaction function. For $G = 0$, neural masses are decoupled, while for increasingly higher values of G their behavior will deviate ever more from the uncoupled scenario.

A successful example of this approach is the study, performed by di Santo and colleagues, of a network of LG neural masses [68] embedded in a 2D square lattice, with the addition of a multiplicative noise and diffusive coupling, resulting in:

$$\begin{aligned} \dot{\rho}_i(t) &= (-a + R_i(t))\rho_i(t) + b\rho_i^2(t) - \rho(t)_i^3 + h + D\nabla^2\rho_i(t) + \sigma\sqrt{\rho_i(t)}n_i(t) \\ \dot{R}_i(t) &= \frac{1}{\tau_R}(\xi - R_i(t)) - \frac{1}{\tau_D}R_i(t)\rho_i(t), \end{aligned} \tag{28}$$

where $\nabla^2\rho_i = \sum_{j \in n.n.i}(\rho_j - \rho_i)$, and the diffusion constant D and the noise coefficient σ are set to 1 without loss of generality. For values of ξ which brought the system to the edge between the oscillation phase and the up-state regime, scale-

invariant avalanches were detected, revealing how this model displays critical behavior at a synchronization phase transition, a crucial difference with previous models which proposed a quiescent-to-active transition.

In conclusion, the core message that can be drawn from the models explored in this chapter is that, to achieve a description of the avalanche phenomenon in a whole-brain network, different modeling scales need to be combined. The network can be represented as a connectome, hosting in every node a mean-field model describing a mesoscale population of neurons. This model can be derived as an approximation of more detailed microscopic models, in which single neurons are considered, as is the case in our work and is discussed in the next chapter.

4 A connectome-based model

In this work, we implemented a connectome-based model, describing the brain as a network of regions (nodes) connected via structural pathways (links). The set of all structural links is provided by the structural connectivity (SC), which can be derived from experiments measuring the number of white-matter tracts (link's weight) connecting any pair of brain regions. Neuronal activity is modeled as a NMM i.e., a set of differential equations describing the mean-field activity of a brain region. A whole-brain simulation consists of NMMs coupled through the SC, and brain dynamics can be obtained by solving the coupled system of differential equations. In the following sections, we describe the details of our connectome-based simulation.

4.1 The structural connectivity

The SC is an N by N matrix whose entries W_{ij} represent the connection strength from region i to j in the chosen brain parcellation, normalized to obtain relative weights such that $W_{ij} \in [0, 1] \; \forall \; i, j$. In this work, we adopted a mouse connectome obtained by processing tracer experiments from the Allen Institute [77] resulting in a directed graph. This graph is generally fully connected, with weight distribution spanning across a wide range: most links are weak, but there are a few strong links that constitute a characteristic structural backbone of the network. Notice that the Allen Institute mouse connectome is obtained from experiments on a large population of $\sim$2000 mice, and therefore it is not "personalized". Other experiments are available for personalized connectomes, such as Diffusion Tensor Imaging (DTI), which can also be performed on humans. However, DTI is generally less precise than tracer experiments and it does not provide information about the structural link directionality.

Here, following up on the work of Melozzi et al. [78], we define the link strength between two brain regions according to the anterograde tracing information provided by the Allen Institute. More in detail, the axonal projections from a localized portion of brain tissue are mapped by injecting in adult male C57Bl/6J mice the recombinant adeno-associated virus, which expresses the EGFP anterograde tracer. The

tracer migration signal is then detected with a serial two-photon tomography system. This approach is repeated systematically to collect information on the tracer migration from several injection sites in the right hemisphere to target regions in both hemispheres, repeating the experiment several times for each injection site.

The Allen Institute provides its data through an internet-accessible interface, namely the Allen Software Development Kit (Allen SDK), from which we retrieved data on all experiments involving brain regions of the parcellation we were interested in, consisting of $N = 92$ regions of the cortex and of the thalamus. The Allen Institute also provides different kinds of data regarding tracer experiments, such as:

- Injection density, Id_i: the fraction of infected voxels in the source region, with respect to the total number of voxels belonging to such region,
- Projection energy, Pe_j: the intensity of detected voxels in the target region normalized with respect to the total number of voxels belonging to that region,
- Projection density, Pd_j: the number of detected pixels in the target region, again normalized with respect to the total voxel number.

We defined the structural weights as $W_{ij} = \overline{Pd_j/Id_i}$, where the mean is performed over all experiments where both source region i and target region j are involved. Doing so, we account for the pervasiveness with which the source communicates with the target as well as for how much the injection of each experiment succeeded in diffusing in the source region. Furthermore, as stated above, experiments of the Allen Institute only consider source regions located in the right hemisphere, therefore, to obtain a complete connectome, we assumed total symmetry between connections starting from the right hemisphere and those starting from the opposite one, an assumption justified by the fact that the mouse brain shows a high degree of lateral symmetry [79]. Hence,

$$\begin{aligned} W_{ij} &= W_{kl} \qquad \forall \;\; k = i + N/2, \;\; l = j + N/2 \\ W_{ij} &= W_{kl} \qquad \forall \;\; k = i + N/2, \;\; j = l + N/2, \end{aligned} \tag{29}$$

assuming regions to be sorted first by hemisphere and then following the same order for the two hemispheres. This effectively amounts to stating that the resulting SC matrix can be divided into four quadrants, where the first and third ones are identical, as are the second and fourth ones. The resulting connectome is shown in Fig. 2.

We confirmed that the weights W_{ij} were approximately distributed across orders of magnitude, following a power law trend with an exponential cutoff (see Fig. 2).

4.2 A layer-specific connectome

The number of brain regions considered, $N = 92$, is limited by the resolution of the experiments. However, a high resolution for the structural connectome is a desirable feature, since the brain—and in particular the cortex—presents a characteristic layered structure that is believed to be fundamental to explaining brain function. In the mouse cortex, anatomical brain regions are divided into 4–6 layers, each presenting different anatomical and thus functional features. With the development of finer technology, the resolution of available data has increased, allowing for the definition of more precise connectomes. While this data is available at the Allen Institute, to our knowledge the full layered connectome was never extracted before. In our work, we

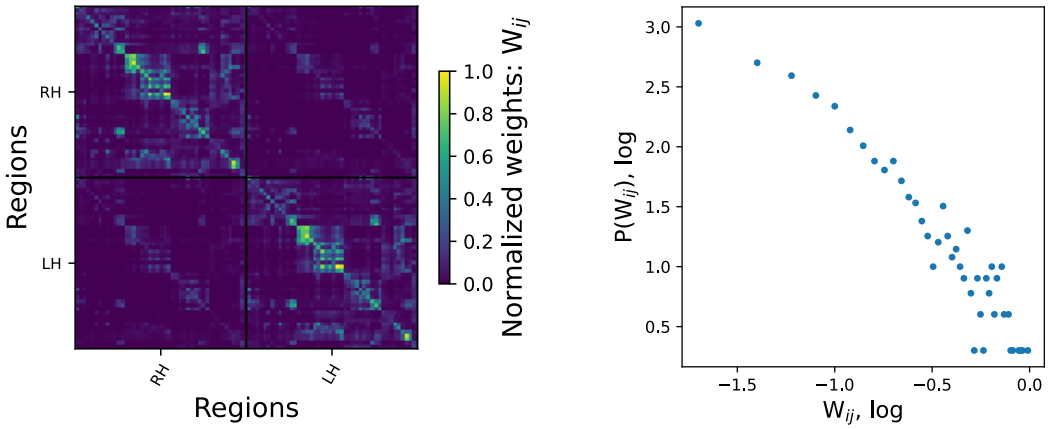

Figure 2: a) Connectome obtained using mouse connectivity data from experiments performed by the Allen Institute for Brain Science; each entry W_{ij} represents the connection strength between two brain regions. b) Distribution of the values of W_{ij}, in a loglog plot.

contributed to this important piece of information by extracting high-precision data from the Allen Institute and building the mouse SC with layer-specific resolution, composed of more than 500 regions. Although we chose not to base our simulations on this finer connectome, owing to the challenge it posed in terms of computational capacity, future work may very well consider its implementation for the sake of more accurate results, e.g., in the search for network-wide critical behavior.

4.3 The model

To simulate cortical activity, we opted for using the same NMM on every site of the network, guided by the simplifying assumption that all portions of cortical tissue can be described by the same model (although regional heterogeneity is an important feature of brain tissues). We chose the mean-field oscillator model derived from Eq. 16 using the OA ansatz, i.e.,

$$\begin{aligned} \dot{R}(t) &= \frac{1}{2}R(t)[J(1-R(t)^2)-\sigma^2] - \frac{1}{2}a(1-R(t)^2)\cos\psi(t) \\ \dot{\psi}(t) &= \omega + \frac{a(1+R(t)^2)\sin\psi(t)}{2R(t)}. \end{aligned} \tag{30}$$

This minimal unit of our model is meant to represent a neuronal population operating around its critical regime. In fact, Buendía and colleagues showed that direct simulations of the neuron-population activity, Eq. 16, displayed critical avalanche behavior at the crossing of the transition line separating the bistability regime from the synchronous-activity phase. Hence, we first looked for the combination of parameters a and σ which would reproduce a bistable regime for the neural mass. To this purpose, we performed 1000 simulations of the time evolution of Eq. 30, spanning the parameter space in the range $a \in [0.75, 1.2]$, $\sigma \in [0.50, 0.80]$.

Furthermore, following up on Buendía's work, we determined analytically the bifurcation lines of the uncoupled unit to identify the bistability region. Results are reported in Fig. 3. In the following, a brief account of the derivation of the bifurcation lines is reported.

The values of ω and J can be fixed to 1 without loss of generality. In the annealed

Kuramoto limit, $a = 0$, the system undergoes a Hopf bifurcation; on the other hand, uncoupled oscillators, i.e., for $J = 0$, exhibit a SNIC bifurcation. Hence, due to the continuity of the solutions, two branches of these two types of bifurcations are expected in the phase diagram. Letting Q be the Jacobian evaluated at a fixed point, at Hopf bifurcations $\mathrm{Tr}(Q) = 0$ while at saddle-node ones $\det(Q) = 0$. Thus, imposing one of these conditions, together with the fixed point definition $\dot{R} = \dot{\psi} = 0$, leads to a set of equations for the parameters of the system as a function of the fixed point values R^* and ψ^*. Since such values are bounded, these equations constitute parametric equations of the bifurcation curve and don't require explicit computation of the values of the fixed points and their stability. With regards to the Hopf bifurcation, solving for $\dot{R} = \dot{\psi} = \mathrm{Tr}(Q) = 0$ leaves three unknowns. Solving for R and $\cos\psi$ turns out to be highly convenient, yielding the parametric curve $a_H(\omega, J, \sigma)$:

$$a_H = \sqrt{\frac{J - \sigma^2}{J + \sigma^2}} \frac{\sqrt{4\omega^2(J + \sigma^2)^2 + J^2(J - \sigma^2)^2}}{2J}. \tag{31}$$

Concerning the saddle-node bifurcation curves, solving $\dot{R} = \dot{\psi} = \det(Q) = 0$ for ω

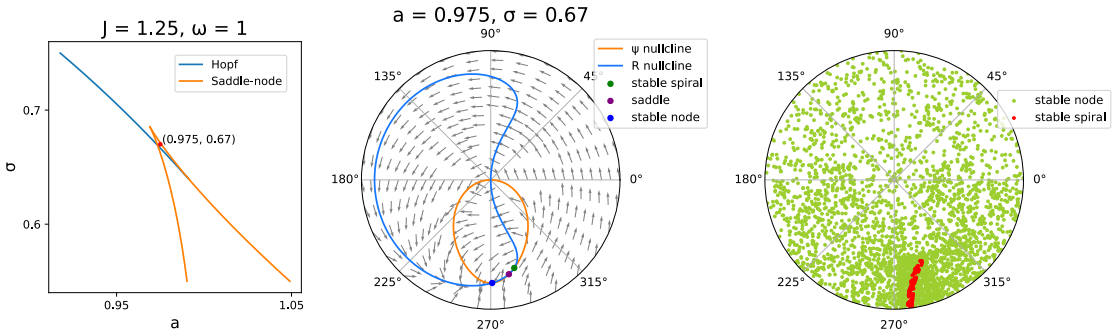

Figure 3: a) Bifurcation lines for the single-unit mean-field model described by Eq. 30, featuring a Hopf bifurcation and two saddle-node lines, as obtained by Eqs. 31 and 32. The red dot highlights the chosen operating point, inside the bistability region. b) Flow in phase space for Eq. 30. The nullclines intersect in two stable points, as expected in the bistability region. c) Attractor basins for the phase space diagram of (b), obtained simulating the time evolution of Eq. 30 with random initial conditions.

and $\cos\psi$ leads to a set of two equations:

$$\begin{aligned} \omega_S &= \frac{(1+R^{*2})^{3/2}}{2(1-R^{*2})^2}\sqrt{J(1-R^{*2})\left(2\sigma^2 - J(1-R^{*2})^2\right) - \sigma^4(1+R^{*2})} \\ a_S &= \frac{\sqrt{2}R^{*2}}{(1-R^{*2})^2}\sqrt{\left(J(1-R^{*2}) - \sigma^2\right)\left(2\sigma^2 - J(1-R^{*2})^2\right)}, \end{aligned} \tag{32}$$

where $R^* \in [0,1]$. Since ω_S is forced to be 1, by exploring all possible values of R, two free parameters are left in the system of equations, which effectively provides a relation for the curves $a_S(\sigma)$.

Merging the results of these two analyses, we chose as values for the parameters $J = 1.25$, to slightly enhance the width of the single-unit bistability region, $\omega = 1$ as in [64], $a = 0.975$ and $\sigma = 0.67$ to tune uncoupled neural masses at the bistability regime.

We then proceeded to simulate more accurately the evolution of an uncoupled neural mass operating at the bistability regime to confirm the expected behavior. Two stable fixed points are present in the phase space: a node and a spiral, as expected in the bistability region. The introduction of additive noise on the second state variable, ψ, produces excursions of the activity from the stable node to the second attractor. Furthermore, depending on noise amplitude, activity can be driven beyond the second point and circle back to the first one, passing close to the origin. The noise intensity necessary to drive activity out of the basin of attraction of the first point ends up also being sufficient to push it out of the second one quite quickly, thus never allowing the system to relax to the second attractor. To identify these rare events, R proves to be a good evaluation parameter, as the two fixed points differ in the value of this variable. Simulation results are reported in Fig. 4.

Having chosen a fully connected weighted graph in which every node obeys the same equations, the model needs just the definition of a coupling function to be complete. To remain coherent with standard oscillator models—a choice operated also by Buendía and colleagues—we opted for a sinusoidal coupling function and additive Gaussian noise, both acting on the second state variable of every unit: its

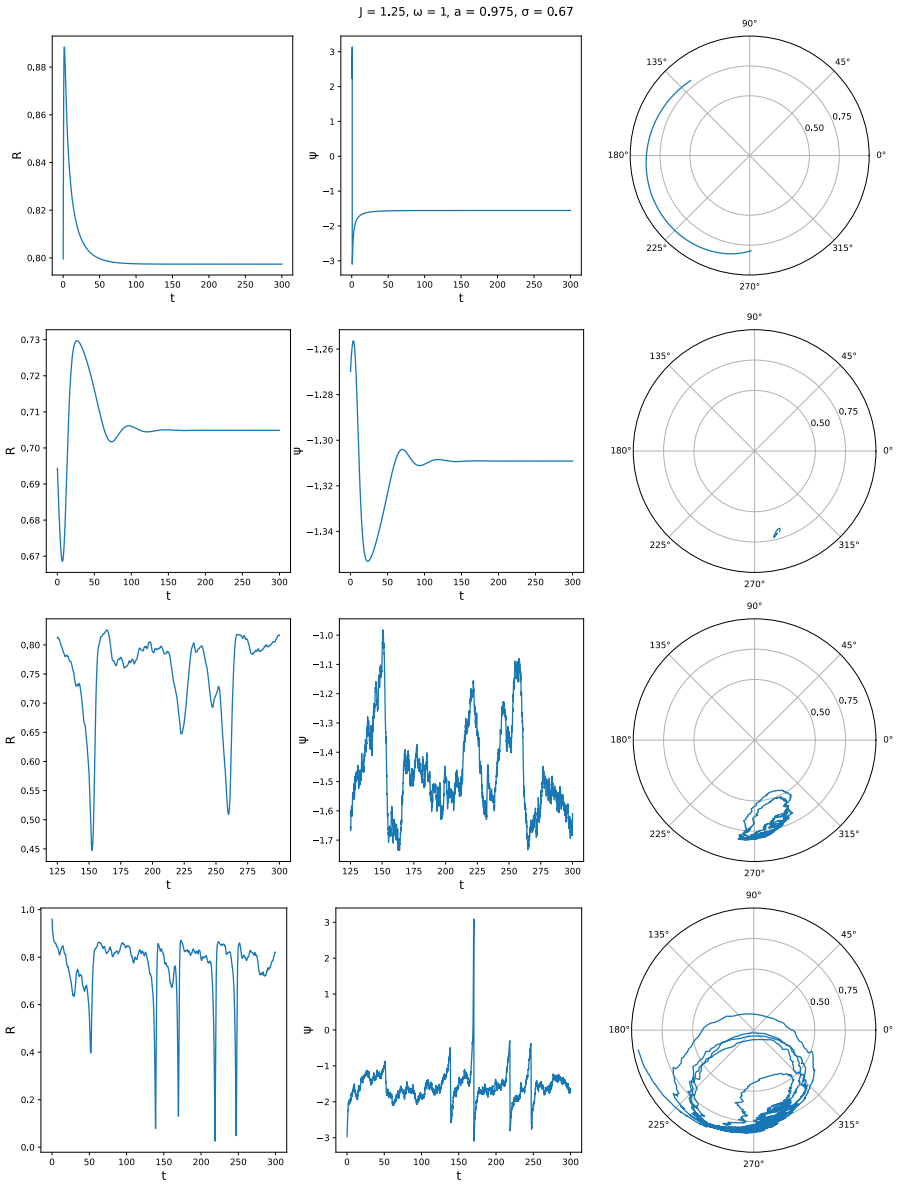

Figure 4: Simulations of the activity of the uncoupled NM, Eq 30. a), b) Noiseless trajectories ending respectively onto the stable node/spiral. c), d) Simulations showing excursions of the activity from the stable node to the second attractor caused by additive noise on state variable ψ. Depending on noise amplitude, activity can be driven beyond this second point and circle back to the first one, passing close to the origin. The graphs show how small values of R allow the identification of such excursions.

phase ψ_i. The full model thus reads:

$$\begin{aligned} \dot{R}_i(t) &= \frac{1}{2}R_i(t)\left[J(1-R_i^2(t))-\sigma^2\right]-\frac{1}{2}a(1-R_i^2(t))\cos\psi_i(t) \\ \dot{\psi}_i(t) &= \omega+\frac{a(1+R_i^2(t))\sin\psi_i(t)}{2R_i(t)}+G\sum_{j=1}^{N}W_{ij}\sin\left[\psi_j(t)-\psi_i(t)\right]+\eta n_i(t), \end{aligned} \tag{33}$$

where $n_i(t)$ is a unit-variance zero-mean Gaussian noise, η is the amplitude of the resulting noise and G is the global coupling strength, which governs how far away from uncoupled-unit dynamics the network evolution will be. G and η are the free parameters explored in our analysis and search for avalanche behavior in the network.

The appropriateness of the chosen coupling function may be verified by simulating the activity of two or more numerous populations of microscopic units, Eq. 16, suitably coupled inter- and intra-population, to compare the results with the simulation of the same number of coupled neural masses; such analysis is left for elsewhere (see section 6.2).

5 Simulating a whole-brain network

In this chapter, readers can find an overview of the methods used in this work to simulate neuronal activity and to analyze the resulting data. Our first objective was to identify values of the parameters G and η for which scale-invariant avalanche behavior emerged at the network level.

We performed all simulations of neuron activity using The Virtual Brain (TVB) [80], a software largely developed and maintained at the host institution in the context of the Human Brain Project, available at the EBRAINS platform. TVB is intended to implement connectome-based simulations of neuronal models and thus supports: the use of a SC as the underlying graph through which units interact; several well-knows NMMs, as well as the possibility to define a custom one; various up-and-running integration schemes, to simulate deterministic time evolution or to include additive or multiplicative noise; the possibility to extract time-averaged data or signals suitable to be compared with neurobiological recordings (e.g., BOLD signals), other than plain state-variable time series. We chose to employ a Heun integrator scheme and to collect all data points for the two state variables of every region, $R_i(t)$ and $\psi_i(t)$. The resulting simulated activity showed spike-like behavior for the state variable R, as shown in Fig. 5.

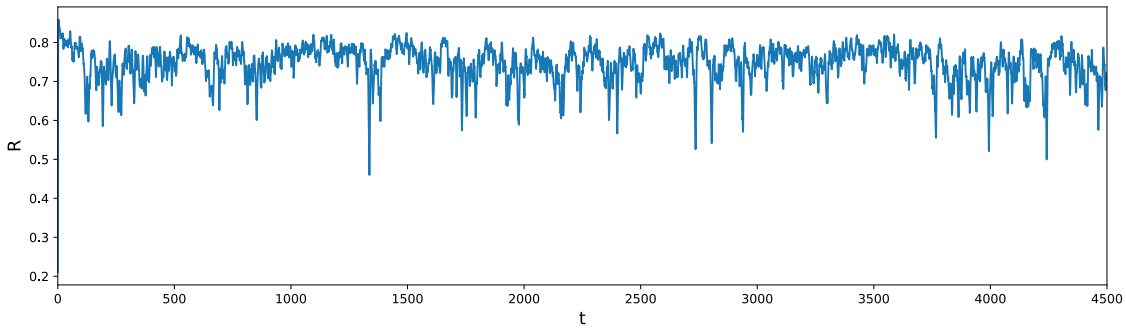

Figure 5: Activity of the first state variable, R, of one node of the simulated network, displaying spike-like behavior.

5.1 Avalanche detection

The protocol implemented to detect avalanches in the simulated network activity closely matches the one described and employed by Buendía et al. to analyze a network of oscillators, which in turn was inspired by the first approach of Beggs and Plenz [12]. An illustrative description of the analysis process is reported in Fig. 6 and its steps can be summarized as follows:

1. An initial transient is discarded. Then, the activity of region i is defined as the z-score of $R_i(t)$, named z_i. This choice was motivated by the observation that single-unit dynamics exhibit bistability and a dynamical evolution concentrated mostly around the first attractor, visiting rarely the second one, as explained in Fig. 4. Thus, the z-score of R proves quite useful to identify these events as the two attractors are positioned at different values for this state variable.

2. A threshold, z_{th}, is chosen to determine when regions are undergoing a "spiking event", i.e., when $|z_i| > z_{th}$. Its value is determined as that which would mark one percent of the total points across all time series as part of an event.

3. The total integral of $|z_i| - z_{th}$ during the above-threshold window is the size s_i^k of the event happening at the initiation time t_k, where k numbers the observed events such that $t_{k+1} \geq t_k \; \forall \, k$. A raster plot for the events can be constructed as a matrix R with entries $R_{t_k,i} = \mathbb{I}[\exists \; s_i^k]$, effectively binarizing event sizes. Here, $\mathbb{I}$ denotes the indicator function of a proposition:

$$\mathbb{I}[A] = 1 \iff A, \;\; \mathbb{I}[A] = 0 \iff \neg A. \tag{34}$$

4. Inter-event intervals are computed as the difference between t_k of all couples of consecutive events and the average inter-event interval, $\langle IEI \rangle$, is computed. Note that multiple t_k could have the same value, in which case they contribute one time each to the distribution of IEI.

5. The event raster is binned over time, using $\langle IEI \rangle$ as bin size. Effectively, sizes s_i^k having t_k belonging to the same time bin are summed.

6. An avalanche is defined as a sequence of contiguous time bins having at least one active region each. Its size, S, will correspond to the sum of all event sizes contributing to the avalanche, while its duration, T, will be the number of bins it consists of. Size and duration of all avalanches are computed. Also, the number of active regions, n_j, for every bin in the avalanche is stored, corresponding to $n_j = \sum_i \mathbb{I}[\exists\ s_i^k \wedge t_k \in bin_j]$, where j numbers the bins.

5.2 Analysis of criticality measures

To analyse the distributions of avalanche metrics, meaning their size, S, and duration, T, we employ a Python package named *powerlaw*, realized by Jeff Alstott and first described in [81]. Owing to the large fluctuations that occur in the tail of the distribution, representing large but rare events, and to the difficulty of identifying the range over which power-law behavior holds, the detection and characterization of power laws is nontrivial. The toolbox we use takes advantage of maximum-likelihood fitting methods with goodness-of-fit tests based on the Kolmogorov-Smirnov statistic, as well as likelihood ratios, to provide a more reliable classification of distributions.

Moreover, as prescribed by the theory on DP, we check the adherence of our findings on critical exponents to the crackling-noise scaling relation, Eq. 6, and we compute the branching parameter from the activity of every simulation. It is defined as:

$$b_p = \sum_d d\ p(d), \tag{35}$$

i.e., the expected value of the observable d, defined as the ratio between the number of active units in a time bin and in its predecessor. This definition is only applicable to couples of contiguous active time bins, thus necessarily belonging to the same avalanche. The distribution of d, $p(d)$, was estimated from activity recordings as:

$$p(d) = \sum_k \mathbb{I}[d_k = d]\ n_a(k), \tag{36}$$

where k indexes all time bins, $d_k = n_a(k+1)/n_a(k)$, and $n_a(k)$ is the number of

active units in the k-th time bin. Under this definition, b_p essentially corresponds to the weighted average of d, where the weights are the number of active regions in every time bin.

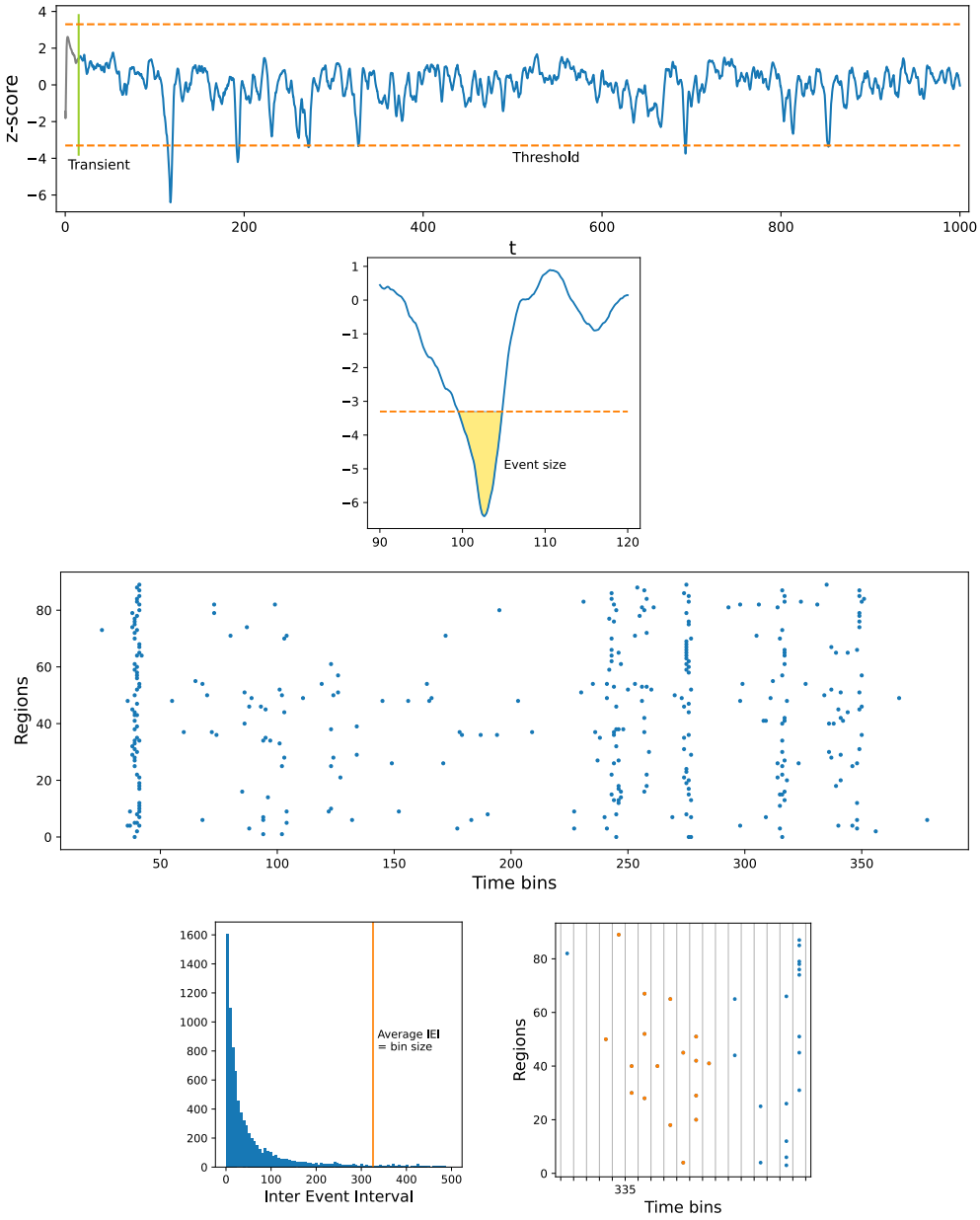

Figure 6: The figures show different steps of the algorithm used to detect avalanches. a) Discarding of an initial transient and z-score thresholding. b) Event identification and integration of the super-threshold signal. c) The resulting event raster. d) Inter-event interval distribution. e) Detection of avalanches and their metrics: size and duration; all data points belonging to one avalanche have been highlighted in orange.

6 Discussion

6.1 Results

In this work, we paved the way for the study of interactions between the critical state of mesoscopic neuron populations and that of the whole brain network they are embedded in.

We first constructed a connectome, or SC, capable of representing realistic white-matter connections between cortical and thalamic regions in the mouse brain, leaving open the possibility of selecting different regions for future analyses.

Secondly, we confirmed the presence of a bistability region in the mean-field oscillator model derived from a modified type-I excitable Kuramoto model [64] using the OA ansatz, identified the values of the parameters a and σ which set the model in the bistable regime, and tested whether it could effectively represent a population of neurons at the edge of a particular synchronization transition, where scale-invariant avalanche behavior emerges alongside incipient oscillations.

We then proceeded to set up a pipeline to simulate network activity and analyze it in search of the values of parameters G and η which produce avalanche behavior, developing methods to identify critical behavior in simulated neuronal activity. We implemented the analysis of avalanche metrics distributions, $p(S) = S^{-\tau}$ and $p(T) = T^{-\alpha}$, evaluating critical exponents τ and α and checking their adherence to theory-provided scaling relations, Eq. 6, as well as computing the branching parameter, b_p. The correspondence of these metrics to known values represents a minimal requirement to identify critical behavior and constitutes the basis for further analysis aimed at clarifying whether a second-order phase transition, or some other mechanism, is at play in the system.

Finally, we computed a layer-specific SC from mouse-tracer data provided by the Allen Institute of Brain Science, which constitutes a high-resolution realistic graph in which simulations of cortical activity can be embedded. To our knowledge, this constitutes the first instance of such a detailed connectome, a tool which can prove useful to implement ever more realistic models to analyze brain activity.

6.2 Future directions

This work leaves many open doors to future development.

In the first place, the chosen coupling function for the full-network model can be the subject of validation tests. As the single-unit NMM is meant to represent an ensemble of type-I excitable Kuramoto oscillators, the activity of two such coupled units can be simulated in parallel to that of two suitably-coupled actual populations (e.g., of 5000 oscillators), to determine whether the two scenarios behave similarly and thus asses the appropriateness of sinusoidal coupling between regions.

Furthermore, the first immediate objective of the pipeline we set up, and described above, is the identification of a regime of global criticality, where scale-free avalanches appear and satisfy all criticality criteria described in section 5.2. Upon identification of the values of the parameters G and η which yield this regime, the critical state of any single node, subject to the network input, can be investigated. This can be done, similarly to the case of the coupling function, simulating directly the population of neurons represented by the node and feeding to it the actual input provided by the network, to analyze its collective behavior and determine whether it is super- (or sub-) critical, and how far from the critical point it is operating at various times.

Finally, the metrics used to assess whether a network is actually operating in a critical state are a crucial point of this work. Maximal care is required in this step, in order not to mistakenly attribute the feature of "critical" to simulated activity. One of the improvements to this classification will be the implementation of shape collapse detection in recorded avalanches. Shape collapse is a phenomenon predicted by field theory, in which the profile of, e.g., the number of active regions over the time bins of an avalanche is described by a scaling function, i.e., a function whose profile is similar for all detected avalanches, upon appropriately rescaling the axis. The identification of this phenomenon can further strengthen the claim that an observed pattern of activity is indeed critical.

These forward steps will allow for a fuller description of the system under study and a deeper analysis of its features, shortening the way to tackle open questions

such as: are critical states related to which regions are most active at a given time? And are RSNs, identified via FC measures, represented in the local critical states of brain regions? Moreover, it has been shown that local alterations (e.g, lesions of a brain region or alteration of the ecxcitation/inhibition rate of neurons inside it) produce change in the network behavior, even at rest. How would such alterations impact on the global critical state, as well as on the local state of other, possibly distant but highly connected, regions?

This and other hypothesis will be tested in the pursuit of the ambitious goal of understanding the *interplay between local and global critical states in the brain.*

References

[1] W Singer and C M Gray. "Visual Feature Integration and the Temporal Correlation Hypothesis". In: *Annual Review of Neuroscience* 18.1 (1995). PMID: 7605074. DOI: 10.1146/annurev.ne.18.030195.003011. eprint: https://doi.org/10.1146/annurev.ne.18.030195.003011. URL: https://doi.org/10.1146/annurev.ne.18.030195.003011.

[2] Andreas K. Engel, Pascal Fries, and Wolf Singer. "Dynamic predictions: Oscillations and synchrony in top–down processing". In: *Nature Reviews Neuroscience* 2.10 (Oct. 2001). ISSN: 1471-003X, 1471-0048. DOI: 10.1038/35094565. URL: https://www.nature.com/articles/35094565.

[3] G.Bard Ermentrout and David Kleinfeld. "Traveling Electrical Waves in Cortex". In: *Neuron* 29.1 (Jan. 2001). ISSN: 08966273. DOI: 10.1016/S0896-6273(01)00178-7. URL: https://linkinghub.elsevier.com/retrieve/pii/S0896627301001787.

[4] Pascal Fries. "A mechanism for cognitive dynamics: neuronal communication through neuronal coherence". In: *Trends in Cognitive Sciences* 9.10 (Oct. 2005), pp. 474–480. ISSN: 13646613. DOI: 10.1016/j.tics.2005.08.011. URL: https://linkinghub.elsevier.com/retrieve/pii/S1364661305002421.

[5] Farnaz Zamani Esfahlani et al. "High-amplitude cofluctuations in cortical activity drive functional connectivity". In: *Proceedings of the National Academy of Sciences* 117.45 (2020).

[6] André M Bastos and Jan-Mathijs Schoffelen. "A tutorial review of functional connectivity analysis methods and their interpretational pitfalls". In: *Frontiers in systems neuroscience* 9 (2016).

[7] Michael D. Fox and Marcus E. Raichle. "Spontaneous fluctuations in brain activity observed with functional magnetic resonance imaging". In: *Nature Reviews Neuroscience* 8.9 (Sept. 2007). ISSN: 1471-003X, 1471-0048. DOI: 10.1038/nrn2201. URL: https://www.nature.com/articles/nrn2201.

[8] J. L. Vincent et al. "Intrinsic functional architecture in the anaesthetized monkey brain". In: *Nature* 447.7140 (May 2007). ISSN: 0028-0836, 1476-4687. DOI: 10.1038/nature05758. URL: https://www.nature.com/articles/nature05758.

[9] Jonathan D. Power et al. "Functional Network Organization of the Human Brain". In: *Neuron* 72.4 (Nov. 2011). ISSN: 08966273. DOI: 10.1016/j.neuron.2011.09.006. URL: https://linkinghub.elsevier.com/retrieve/pii/S0896627311007926.

[10] Giovanni Rabuffo et al. "Neuronal Cascades Shape Whole-Brain Functional Dynamics at Rest". In: *eNeuro* 8.5 (2021). DOI: 10.1523/ENEURO.0283-21.2021. eprint: https://www.eneuro.org/content/8/5/ENEURO.0283-21.2021.full.pdf. URL: https://www.eneuro.org/content/8/5/ENEURO.0283-21.2021.

[11] Nikolai F. Rulkov and Maxim Bazhenov. "Oscillations and Synchrony in Large-scale Cortical Network Models". In: *Journal of Biological Physics* 34.3-4 (Aug. 2008). ISSN: 0092-0606, 1573-0689. DOI: 10.1007/s10867-008-9079-y. URL: http://link.springer.com/10.1007/s10867-008-9079-y.

[12] John M. Beggs and Dietmar Plenz. "Neuronal Avalanches in Neocortical Circuits". In: *The Journal of Neuroscience* 23.35 (Dec. 2003). ISSN: 0270-6474, 1529-2401. DOI: 10.1523/JNEUROSCI.23-35-11167.2003. URL: https://www.jneurosci.org/lookup/doi/10.1523/JNEUROSCI.23-35-11167.2003.

[13] Maya Paczuski and Stefan Boettcher. "Avalanches and waves in the Abelian sandpile model". In: *Physical Review E* 56.4 (Oct. 1997). ISSN: 1095-3787. DOI: 10.1103/physreve.56.r3745. URL: http://dx.doi.org/10.1103/PhysRevE.56.R3745.

[14] Richter CF Gutenberg B. "Seismicity of the earth". In: *Princeton, NJ: Princeton UP* (1956).

[15] Bruce Malamud, Gleb Morein, and Donald Turcotte. "Forest Fires: An Example of Self-Organized Critical Behavior". In: *Science (New York, N.Y.)* 281 (Oct. 1998). DOI: 10.1126/science.281.5384.1840.

[16] Stefano Zapperi, Kent Bækgaard Lauritsen, and H. Eugene Stanley. "Self-Organized Branching Processes: Mean-Field Theory for Avalanches". In: *Physical Review Letters* 75.22 (Nov. 1995). DOI: 10.1103/physrevlett.75.4071. URL: https://doi.org/10.1103%2Fphysrevlett.75.4071.

[17] Woodrow L. Shew et al. "Information Capacity and Transmission Are Maximized in Balanced Cortical Networks with Neuronal Avalanches". In: *Journal of Neuroscience* 31.1 (2011). ISSN: 0270-6474. DOI: 10.1523/JNEUROSCI.4637-10.2011. eprint: https://www.jneurosci.org/content/31/1/55.full.pdf. URL: https://www.jneurosci.org/content/31/1/55.

[18] Woodrow L. Shew and Dietmar Plenz. "The Functional Benefits of Criticality in the Cortex". In: *The Neuroscientist* 19.1 (Feb. 2013). ISSN: 1073-8584, 1089-4098. DOI: 10.1177/1073858412445487. URL: http://journals.sagepub.com/doi/10.1177/1073858412445487.

[19] Osame Kinouchi and Mauro Copelli. "Optimal dynamical range of excitable networks at criticality". In: *Nature Physics* 2.5 (May 2006). ISSN: 1745-2473, 1745-2481. DOI: 10.1038/nphys289. URL: https://www.nature.com/articles/nphys289.

[20] Daniel B. Larremore, Woodrow L. Shew, and Juan G. Restrepo. "Predicting Criticality and Dynamic Range in Complex Networks: Effects of Topology". In: *Physical Review Letters* 106.5 (Jan. 2011). ISSN: 0031-9007, 1079-7114. DOI: 10.1103/PhysRevLett.106.058101. URL: https://link.aps.org/doi/10.1103/PhysRevLett.106.058101.

[21] Emmanuelle Tognoli and J. A. Scott Kelso. "The Metastable Brain". In: *Neuron* 81.1 (Jan. 2014). ISSN: 08966273. DOI: 10.1016/j.neuron.2013.12.022. URL: https://linkinghub.elsevier.com/retrieve/pii/S0896627313011835.

[22] Alberto Mazzoni et al. "On the Dynamics of the Spontaneous Activity in Neuronal Networks". In: *PLoS ONE* 2.5 (May 2007). Ed. by Olaf Sporns. ISSN: 1932-6203. DOI: 10.1371/journal.pone.0000439. URL: https://dx.plos.org/10.1371/journal.pone.0000439.

[23] V. Pasquale et al. "Self-organization and neuronal avalanches in networks of dissociated cortical neurons". In: *Neuroscience* 153.4 (June 2008). ISSN: 03064522. DOI: 10.1016/j.neuroscience.2008.03.050. URL: https://linkinghub.elsevier.com/retrieve/pii/S0306452208004028.

[24] Joshua Milstein et al. "Neuronal Shot Noise and Brownian 1/f2 Behavior in the Local Field Potential". In: *PLoS ONE* 4.2 (Feb. 2009). Ed. by Liset Menendez De La Prida. ISSN: 1932-6203. DOI: 10.1371/journal.pone.0004338. URL: https://dx.plos.org/10.1371/journal.pone.0004338.

[25] Nir Friedman et al. "Universal Critical Dynamics in High Resolution Neuronal Avalanche Data". In: *Physical Review Letters* 108.20 (May 2012). ISSN: 0031-9007, 1079-7114. DOI: 10.1103/PhysRevLett.108.208102. URL: https://link.aps.org/doi/10.1103/PhysRevLett.108.208102.

[26] Biyu J. He et al. "The Temporal Structures and Functional Significance of Scale-free Brain Activity". In: *Neuron* 66.3 (May 2010). ISSN: 08966273. DOI: 10.1016/j.neuron.2010.04.020. URL: https://linkinghub.elsevier.com/retrieve/pii/S0896627310002916.

[27] Nima Dehghani et al. "Comparative power spectral analysis of simultaneous elecroencephalographic and magnetoencephalographic recordings in humans suggests non-resistive extracellular media". In: *Journal of Computational Neuroscience* 29.3 (Dec. 2010). ISSN: 0929-5313, 1573-6873. DOI: 10.1007/s10827-010-0263-2. URL: http://link.springer.com/10.1007/s10827-010-0263-2.

[28] J. Matias Palva et al. "Neuronal long-range temporal correlations and avalanche dynamics are correlated with behavioral scaling laws". In: *Proceedings of the National Academy of Sciences* 110.9 (Feb. 2013). ISSN: 0027-8424, 1091-6490. DOI: 10.1073/pnas.1216855110. URL: https://pnas.org/doi/full/10.1073/pnas.1216855110.

[29] Oren Shriki et al. "Neuronal Avalanches in the Resting MEG of the Human Brain". In: *The Journal of Neuroscience* 33.16 (Apr. 2013). ISSN: 0270-6474, 1529-2401. DOI: 10.1523/JNEUROSCI.4286-12.2013. URL: https://www.jneurosci.org/lookup/doi/10.1523/JNEUROSCI.4286-12.2013.

[30] Biyu J. He. "Scale-Free Properties of the Functional Magnetic Resonance Imaging Signal during Rest and Task". In: *The Journal of Neuroscience* 31.39 (Sept. 2011). ISSN: 0270-6474, 1529-2401. DOI: 10.1523/JNEUROSCI.2111-11.2011. URL: https://www.jneurosci.org/lookup/doi/10.1523/JNEUROSCI.2111-11.2011.

[31] Enzo Tagliazucchi et al. "Criticality in Large-Scale Brain fMRI Dynamics Unveiled by a Novel Point Process Analysis". In: *Frontiers in Physiology* 3 (2012). ISSN: 1664-042X. DOI: 10.3389/fphys.2012.00015. URL: http://journal.frontiersin.org/article/10.3389/fphys.2012.00015/abstract.

[32] P Ciuciu. "Scale-free and multifractal time dynamics of fMRI signals during rest and task". In: *Frontiers in Physiology* 3 (2012). ISSN: 1664042X. DOI: 10.3389/fphys.2012.00186. URL: http://journal.frontiersin.org/article/10.3389/fphys.2012.00186/abstract.

[33] Adrián Ponce-Alvarez et al. "Whole-Brain Neuronal Activity Displays Crackling Noise Dynamics". In: *Neuron* 100.6 (Dec. 2018). ISSN: 08966273. DOI: 10.1016/j.neuron.2018.10.045. URL: https://linkinghub.elsevier.com/retrieve/pii/S089662731830953X.

[34] Ernest Montbrió, Diego Pazó, and Alex Roxin. "Macroscopic Description for Networks of Spiking Neurons". In: *Phys. Rev. X* 5 (2 June 2015). DOI: 10.1103/PhysRevX.5.021028. URL: https://link.aps.org/doi/10.1103/PhysRevX.5.021028.

[35] Abhirup Bandyopadhyay et al. *Mean-field approximation of network of biophysical neurons driven by conductance-based ion exchange*. preprint. Neuroscience, Nov. 2021. DOI: 10.1101/2021.10.29.466427. URL: http://biorxiv.org/lookup/doi/10.1101/2021.10.29.466427.

[36] Dan-Mei Chen et al. "Self-organized criticality in a cellular automaton model of pulse-coupled integrate-and-fire neurons". In: *Journal of Physics A: Mathematical and General* 28.18 (Sept. 1995). ISSN: 0305-4470, 1361-6447. DOI: 10.1088/0305-4470/28/18/009. URL: https://iopscience.iop.org/article/10.1088/0305-4470/28/18/009.

[37] Álvaro Corral et al. "Self-Organized Criticality and Synchronization in a Lattice Model of Integrate-and-Fire Oscillators". In: *Phys. Rev. Lett.* 74 (1 Jan. 1995). DOI: 10.1103/PhysRevLett.74.118. URL: https://link.aps.org/doi/10.1103/PhysRevLett.74.118.

[38] Andreas V. M. Herz and John J. Hopfield. "Earthquake Cycles and Neural Reverberations: Collective Oscillations in Systems with Pulse-Coupled Threshold Elements". In: *Phys. Rev. Lett.* 75 (6 Aug. 1995). DOI: 10.1103/PhysRevLett.75.1222. URL: https://link.aps.org/doi/10.1103/PhysRevLett.75.1222.

[39] Christian W. Eurich, J. Michael Herrmann, and Udo A. Ernst. "Finite-size effects of avalanche dynamics". In: *Phys. Rev. E* 66 (6 Dec. 2002). DOI: 10.1103/PhysRevE.66.066137. URL: https://link.aps.org/doi/10.1103/PhysRevE.66.066137.

[40] Per Bak, Chao Tang, and Kurt Wiesenfeld. "Self-organized criticality: An explanation of the 1/f noise". In: *Phys. Rev. Lett.* 59 (4 July 1987). DOI: 10.1103/PhysRevLett.59.381. URL: https://link.aps.org/doi/10.1103/PhysRevLett.59.381.

[41] Antonio J. Fontenele et al. *Low dimensional criticality embedded in high dimensional awake brain dynamics*. preprint. Neuroscience, Jan. 2023. DOI: 10.1101/2023.01.05.522896. URL: http://biorxiv.org/lookup/doi/10.1101/2023.01.05.522896.

[42] Alessandro Vespignani et al. "Absorbing-state phase transitions in fixed-energy sandpiles". In: *Phys. Rev. E* 62 (4 Oct. 2000). DOI: 10.1103/PhysRevE.62.4564. URL: https://link.aps.org/doi/10.1103/PhysRevE.62.4564.

[43] Siegfried Clar, Barbara Drossel, and Franz Schwabl. "Self-Organized Critical and Synchronized States in a Nonequilibrium Percolation Model". In: *Physical Review Letters* 75.14 (Oct. 1995). ISSN: 0031-9007, 1079-7114. DOI: 10.1103/PhysRevLett.75.2722. URL: https://link.aps.org/doi/10.1103/PhysRevLett.75.2722.

[44] Henrik Jeldtoft Jensen. *Self-organized criticality: emergent complex behavior in physical and biological systems*. Cambridge, UK: Cambridge University Press, 1998.

[45] H. K. Janssen. "On the nonequilibrium phase transition in reaction-diffusion systems with an absorbing stationary state". In: *Zeitschrift för Physik B Condensed Matter* 42.2 (June 1981). ISSN: 0340-224X, 1434-6036. DOI: 10.1007/BF01319549. URL: http://link.springer.com/10.1007/BF01319549.

[46] P. Grassberger. "On phase transitions in Schlögl's second model". In: *Zeitschrift för Physik B Condensed Matter* 47.4 (Dec. 1982). ISSN: 0722-3277, 1434-6036. DOI: 10.1007/BF01313803. URL: http://link.springer.com/10.1007/BF01313803.

[47] Marro J. and Dickman R. *Nonequilibrium Phase Transition in Lattice Models*. Cambridge: Cambridge University Press, 1999.

[48] Jonathan Touboul and Alain Destexhe. "Power-law statistics and universal scaling in the absence of criticality". In: *Physical Review E* 95.1 (Jan. 2017). ISSN: 2470-0045, 2470-0053. DOI: 10.1103/PhysRevE.95.012413. URL: https://link.aps.org/doi/10.1103/PhysRevE.95.012413.

[49] James P. Sethna, Karin A. Dahmen, and Christopher R. Myers. "Crackling noise". In: *Nature* 410.6825 (Mar. 2001). DOI: 10.1038/35065675. URL: https://doi.org/10.1038%2F35065675.

[50] Gregory Scott et al. "Voltage Imaging of Waking Mouse Cortex Reveals Emergence of Critical Neuronal Dynamics". In: *The Journal of Neuroscience* 34.50 (Dec. 2014). ISSN: 0270-6474, 1529-2401. DOI: 10.1523/JNEUROSCI.3474-14.2014. URL: https://www.jneurosci.org/lookup/doi/10.1523/JNEUROSCI.3474-14.2014.

[51] Timothy Bellay et al. "Irregular spiking of pyramidal neurons organizes as scale-invariant neuronal avalanches in the awake state". In: *eLife* 4 (July 2015). ISSN: 2050-084X. DOI: 10.7554/eLife.07224. URL: https://elifesciences.org/articles/07224.

[52] Woodrow L. Shew et al. "Adaptation to sensory input tunes visual cortex to criticality". In: *Nature Physics* 11.8 (Aug. 2015). ISSN: 1745-2473, 1745-2481. DOI: 10.1038/nphys3370. URL: https://www.nature.com/articles/nphys3370.

[53] Tiago L. Ribeiro et al. "Spike Avalanches Exhibit Universal Dynamics across the Sleep-Wake Cycle". In: *PLoS ONE* 5.11 (Nov. 2010). Ed. by Olaf Sporns. ISSN: 1932-6203. DOI: 10.1371/journal.pone.0014129. URL: https://dx.plos.org/10.1371/journal.pone.0014129.

[54] Alexander Zhigalov et al. "Relationship of Fast- and Slow-Timescale Neuronal Dynamics in Human MEG and SEEG". In: *The Journal of Neuroscience* 35.13 (Apr. 2015). ISSN: 0270-6474, 1529-2401. DOI: 10.1523/JNEUROSCI.4880-14.2015. URL: https://www.jneurosci.org/lookup/doi/10.1523/JNEUROSCI.4880-14.2015.

[55] Tawan T. A. Carvalho et al. "Subsampled Directed-Percolation Models Explain Scaling Relations Experimentally Observed in the Brain". In: *Frontiers in Neural Circuits* 14 (Jan. 2021). ISSN: 1662-5110. DOI: 10.3389/fncir.2020.576727. URL: https://www.frontiersin.org/articles/10.3389/fncir.2020.576727/full.

[56] A. Levina, J. M. Herrmann, and T. Geisel. "Dynamical synapses causing self-organized criticality in neural networks". In: *Nature Physics* 3.12 (Nov. 2007). ISSN: 1745-2481. DOI: 10.1038/nphys758. URL: http://dx.doi.org/10.1038/nphys758.

[57] Nigel Stepp, Dietmar Plenz, and Narayan Srinivasa. "Synaptic Plasticity Enables Adaptive Self-Tuning Critical Networks". In: *PLOS Computational Biology* 11.1 (Jan. 2015). Ed. by Wolfgang Einhäuser. ISSN: 1553-7358. DOI: 10.1371/journal.pcbi.1004043. URL: https://dx.plos.org/10.1371/journal.pcbi.1004043.

[58] Nils Bertschinger and Thomas Natschläger. "Real-Time Computation at the Edge of Chaos in Recurrent Neural Networks". In: *Neural Computation* 16.7 (July 2004). ISSN: 0899-7667, 1530-888X. DOI: 10.1162/089976604323057443. URL: https://direct.mit.edu/neco/article/16/7/1413-1436/6890.

[59] Clayton Haldeman and John M. Beggs. "Critical Branching Captures Activity in Living Neural Networks and Maximizes the Number of Metastable States". In: *Physical Review Letters* 94.5 (Feb. 2005). ISSN: 0031-9007, 1079-7114. DOI: 10.1103/PhysRevLett.94.058101. URL: https://link.aps.org/doi/10.1103/PhysRevLett.94.058101.

[60] Wolfgang Maass, Thomas Natschläger, and Henry Markram. "Real-Time Computing Without Stable States: A New Framework for Neural Computation Based on Perturbations". In: *Neural Computation* 14.11 (Nov. 2002). ISSN: 0899-7667, 1530-888X. DOI: 10.1162/089976602760407955. URL: https://direct.mit.edu/neco/article/14/11/2531-2560/6650.

[61] Woodrow L. Shew et al. "Information Capacity and Transmission Are Maximized in Balanced Cortical Networks with Neuronal Avalanches". In: *The Journal of Neuroscience* 31.1 (Jan. 2011). ISSN: 0270-6474, 1529-2401. DOI: 10.1523/JNEUROSCI.4637-10.2011. URL: https://www.jneurosci.org/lookup/doi/10.1523/JNEUROSCI.4637-10.2011.

[62] Juan A. Acebrón et al. "The Kuramoto model: A simple paradigm for synchronization phenomena". In: *Rev. Mod. Phys.* 77 (1 Apr. 2005). DOI: 10.1103/RevModPhys.77.137. URL: https://link.aps.org/doi/10.1103/RevModPhys.77.137.

[63] Yoshiki Kuramoto. "Self-entrainment of a population of coupled non-linear oscillators". In: *International Symposium on Mathematical Problems in Theoretical Physics*. Ed. by Huzihiro Araki. Berlin, Heidelberg: Springer Berlin Heidelberg, 1975. ISBN: 978-3-540-37509-8.

[64] Victor Buendía et al. "Hybrid-type synchronization transitions: Where incipient oscillations, scale-free avalanches, and bistability live together". In: *Phys. Rev. Res.* 3 (2 June 2021). DOI: 10.1103/PhysRevResearch.3.023224. URL: https://link.aps.org/doi/10.1103/PhysRevResearch.3.023224.

[65] Eugene M. Izikevič. *Dynamical systems in neuroscience: the geometry of excitability and bursting*. First MIT Press paperback edition. Computational neuroscience. Cambridge, Massachusetts London, England: The MIT Press, 2010.

[66] B Lindner. "Effects of noise in excitable systems". In: *Physics Reports* 392.6 (Mar. 2004). ISSN: 03701573. DOI: 10.1016/j.physrep.2003.10.015. URL: https://linkinghub.elsevier.com/retrieve/pii/S0370157303004228.

[67] Steven A. Prescott. "Excitability: Types I, II, and III". In: *Encyclopedia of Computational Neuroscience*. Ed. by Dieter Jaeger and Ranu Jung. New York, NY: Springer New York, 2013. ISBN: 978-1-4614-7320-6. DOI: 10.1007/978-1-4614-7320-6_151-1. URL: https://doi.org/10.1007/978-1-4614-7320-6_151-1.

[68] Serena di Santo et al. “Landau–Ginzburg theory of cortex dynamics: Scale-free avalanches emerge at the edge of synchronization”. In: *Proceedings of the National Academy of Sciences* 115.7 (Jan. 2018). ISSN: 1091-6490. DOI: 10.1073/pnas.1712989115. URL: http://dx.doi.org/10.1073/pnas.1712989115.

[69] Hugh R. Wilson and Jack D. Cowan. “Excitatory and Inhibitory Interactions in Localized Populations of Model Neurons”. In: *Biophysical Journal* 12.1 (Jan. 1972). ISSN: 00063495. DOI: 10.1016/S0006-3495(72)86068-5. URL: https://linkinghub.elsevier.com/retrieve/pii/S0006349572860685.

[70] Misha V. Tsodyks and Henry Markram. “The neural code between neocortical pyramidal neurons depends on neurotransmitter release probability”. In: *Proceedings of the National Academy of Sciences* 94.2 (Jan. 1997). ISSN: 0027-8424, 1091-6490. DOI: 10.1073/pnas.94.2.719. URL: https://pnas.org/doi/full/10.1073/pnas.94.2.719.

[71] Irina V. Tyulkina et al. “Dynamics of Noisy Oscillator Populations beyond the Ott-Antonsen Ansatz”. In: *Phys. Rev. Lett.* 120 (26 June 2018). DOI: 10.1103/PhysRevLett.120.264101. URL: https://link.aps.org/doi/10.1103/PhysRevLett.120.264101.

[72] Lauren M. Childs and Steven H. Strogatz. “Stability diagram for the forced Kuramoto model”. In: *Chaos: An Interdisciplinary Journal of Nonlinear Science* 18.4 (Dec. 2008). ISSN: 1089-7682. DOI: 10.1063/1.3049136. URL: http://dx.doi.org/10.1063/1.3049136.

[73] Roman M. Borisyuk and Alexandr B. Kirillov. “Bifurcation analysis of a neural network model”. In: *Biological Cybernetics* 66.4 (Feb. 1992). ISSN: 0340-1200, 1432-0770. DOI: 10.1007/BF00203668. URL: http://link.springer.com/10.1007/BF00203668.

[74] Italo’Ivo Lima Dias Pinto and Mauro Copelli. “Oscillations and collective excitability in a model of stochastic neurons under excitatory and inhibitory coupling”. In: *Phys. Rev. E* 100 (6 Dec. 2019). DOI: 10.1103/PhysRevE.100.062416. URL: https://link.aps.org/doi/10.1103/PhysRevE.100.062416.

[75] Junhao Liang, Tianshou Zhou, and Changsong Zhou. “Hopf Bifurcation in Mean Field Explains Critical Avalanches in Excitation-Inhibition Balanced Neuronal Networks: A Mechanism for Multiscale Variability”. In: *Frontiers in Systems Neuroscience* 14 (Nov. 2020). ISSN: 1662-5137. DOI: 10.3389/fnsys.2020.580011. URL: https://www.frontiersin.org/articles/10.3389/fnsys.2020.580011/full.

[76] Serena di Santo et al. “Simple unified view of branching process statistics: Random walks in balanced logarithmic potentials”. In: *Phys. Rev. E* 95 (3 Mar. 2017). DOI: 10.1103/PhysRevE.95.032115. URL: https://link.aps.org/doi/10.1103/PhysRevE.95.032115.

[77] Seung Wook Oh et al. “A mesoscale connectome of the mouse brain”. In: *Nature* 508.7495 (Apr. 2014). ISSN: 0028-0836, 1476-4687. DOI: 10.1038/nature13186. URL: https://www.nature.com/articles/nature13186.

[78] Francesca Melozzi et al. “The Virtual Mouse Brain: A Computational Neuroinformatics Platform to Study Whole Mouse Brain Dynamics”. In: *eneuro* 4.3 (May 2017). ISSN: 2373-2822. DOI: 10.1523/ENEURO.0111-17.2017. URL: https://www.eneuro.org/lookup/doi/10.1523/ENEURO.0111-17.2017.

[79] Evan Calabrese et al. “A Diffusion MRI Tractography Connectome of the Mouse Brain and Comparison with Neuronal Tracer Data”. In: *Cerebral Cortex* 25.11 (Nov. 2015). ISSN: 1047-3211, 1460-2199. DOI: 10.1093/cercor/bhv121. URL: https://academic.oup.com/cercor/article-lookup/doi/10.1093/cercor/bhv121.

[80] Paula Sanz Leon et al. “The Virtual Brain: a simulator of primate brain network dynamics”. In: *Frontiers in Neuroinformatics* 7 (2013). ISSN: 1662-5196. DOI: 10.3389/fninf.2013.00010. URL: https://www.frontiersin.org/articles/10.3389/fninf.2013.00010.

[81] Aaron Clauset, Cosma Rohilla Shalizi, and M. E. J. Newman. “Power-Law Distributions in Empirical Data”. In: *SIAM Review* 51.4 (Nov. 2009). ISSN: 1095-7200. DOI: 10.1137/070710111. URL: http://dx.doi.org/10.1137/070710111.